HHS Public Access

Author manuscript

Cell Rep. Author manuscript; available in PMC 2024 July 12.

Published in final edited form as:

Cell Rep. 2024 May 28; 43(5): 114117. doi:10.1016/j.celrep.2024.114117.

Altered GM1 catabolism affects NMDAR-mediated Ca^{2+} signaling at ER-PM junctions and increases synaptic spine formation in a GM1-gangliosidosis model

Jason A. Weesner[1], **Ida Annunziata**[1,2], **Diantha van de Vlekkert**[1], **Camenzind G. Robinson**[3], **Yvan Campos**[1], **Ashutosh Mishra**[4], **Leigh E. Fremuth**[1], **Elida Gomero**[1], **Huimin Hu**[1], **Alessandra d'Azzo**[1,5,6,*]

[1]St. Jude Children's Research Hospital, Department of Genetics, Memphis, TN 38105, USA

[2]St. Jude Children's Research Hospital, Compliance Office, Memphis, TN 38105, USA

[3]St. Jude Children's Research Hospital, Cellular Imaging Shared Resource, Memphis, TN 38105, USA

[4]St. Jude Children's Research Hospital, Center for Proteomics and Metabolomics, Memphis, TN 38105, USA

[5]University of Tennessee Health Science Center, Department of Anatomy and Physiology, Memphis, TN 38163, USA

[6]Lead contact

SUMMARY

Endoplasmic reticulum-plasma membrane (ER-PM) junctions mediate Ca^{2+} flux across neuronal membranes. The properties of these membrane contact sites are defined by their lipid content, but little attention has been given to glycosphingolipids (GSLs). Here, we show that GM1-ganglioside, an abundant GSL in neuronal membranes, is integral to ER-PM junctions; it interacts with synaptic proteins/receptors and regulates Ca^{2+} signaling. In a model of the neurodegenerative lysosomal storage disease, GM1-gangliosidosis, pathogenic accumulation of GM1 at ER-PM junctions due to β-galactosidase deficiency drastically alters neuronal Ca^{2+} homeostasis. Mechanistically, we show that GM1 interacts with the phosphorylated N-methyl D-aspartate receptor (NMDAR) Ca^{2+} channel, thereby increasing Ca^{2+} flux, activating extracellular signal-regulated kinase (ERK) signaling, and increasing the number of synaptic spines without

*Correspondence: sandra.dazzo@stjude.org.

AUTHOR CONTRIBUTIONS

A.d'A. conceived and designed the study and edited the manuscript. J.A.W. designed the experiments, collected and analyzed data, and drafted the manuscript. I.A. coordinated the experimental design and edited the first draft. D.v.d.V. edited the STAR Methods and formatted all figures and graphical abstract. C.G.R. performed TEM analyses and assisted in data interpretation. Y.C. produced the lentivirus constructs. A.M. performed proteomic analyses. L.E.F. reviewed the manuscript and assisted with experiments. H.H. performed histopathologic analyses. E.G. helped collect animal tissues and maintained the animal colony. All authors have read and agreed to the published version of the manuscript.

DECLARATION OF INTERESTS

The authors declare no competing interests.

SUPPLEMENTAL INFORMATION

Supplemental information can be found online at https://doi.org/10.1016/j.celrep.2024.114117.

increasing synaptic connectivity. Thus, GM1 clustering at ER-PM junctions alters synaptic plasticity and worsens the generalized neuronal cell death characteristic of GM1-gangliosidosis.

In brief

Weesner et al. find that, in GM1-gangliosidosis mice, neuronal accumulation of GM1 at the ER-PM junctions alters NMDAR-mediated Ca^{2+} signaling and activates the synaptogenesis pathway via ERK signaling. This leads to increased synaptic spine density without an increase in synaptic connectivity, contributing to the neurodegeneration characteristic of the disease.

Graphical abstract

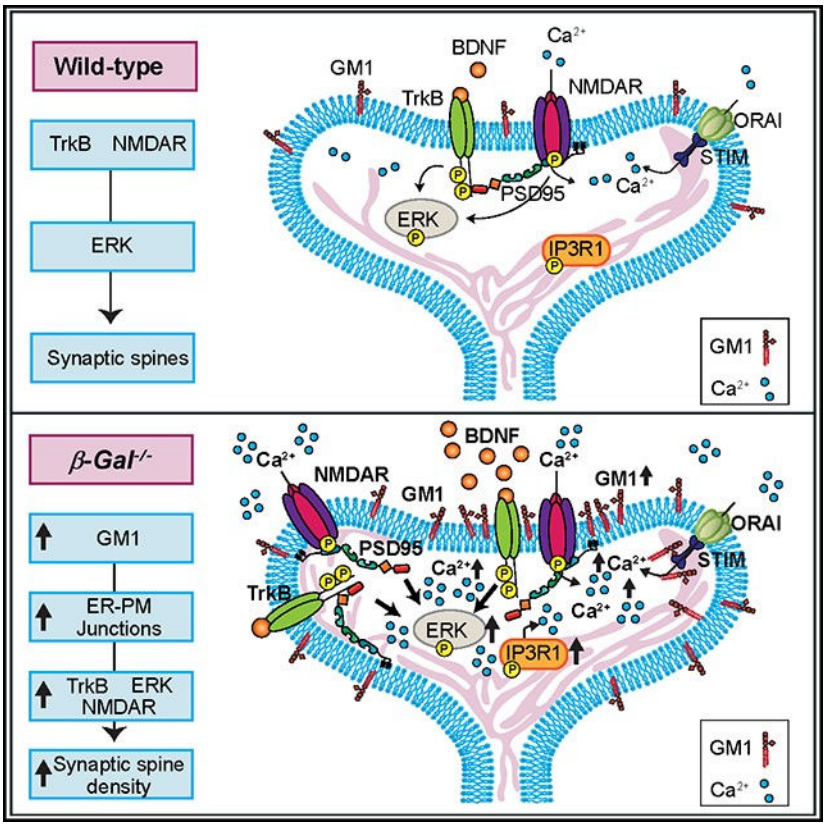

INTRODUCTION

In eukaryotes, communication among intracellular organelles or with the cell's exterior is a prerequisite for cells to adapt their dynamic metabolic needs and respond to diverse physiologic or pathologic cues.[1] One universal mode of communication is through membrane contact sites (MCSs), which represent areas of juxtaposition between organellar membranes and/or the plasma membrane (PM), keeping an average distance of ~10–35 nm.[2,3] MCSs form transiently and reversibly by tethering membrane proteins or protein complexes and lipids, creating specialized "hit-and-run" signaling platforms that coordinate the synthesis/transport of lipids, the exchange of ions and metabolites (e.g., Ca^{2+}, and other metabolic processes that do not require membrane fusion or vesicular trafficking.[4–7]

The extensive membrane network of the endoplasmic reticulum (ER) makes contacts with virtually all other intracellular organelles and the PM.[4,8] The latter are referred to as ER-PM junctions.[9] These MCSs, first visualized on electron micrographs of muscle cells,[10] occur frequently in neurons, where the highly polarized membranes may require ER-PM junctions to enable efficient synaptic communication.[11–13] Notably, a comprehensive analysis of the ER distribution in mouse brain tissue revealed that ER cisternae extend throughout the neuronal cell body, axons, and dendritic arbors, and they penetrate both the postsynaptic dendritic spines and the presynaptic axon terminals.[12] The quantity and type of synapses depend on the size, shape, and number of the dendritic spines, which are highly plastic and subjected to changes in response to neuronal activity.[14,15] Two major classes of spines, large mushroom-shaped spines and thin-shaped spines, are controlled by the quantity and distribution of two glutamate receptors, N-methyl D-aspartate receptors (NMDARs) and α-amino-3-hydroxy-5-methyl-4-isoxazolepropionate receptors (AMPARs), which are integral to neuroplasticity at excitatory synapses.[15–17] Both receptors serve as ion channels, and their recruitment to or removal from the PM depends on their phosphorylation status and changes in flux at the postsynaptic terminal.[18,19] The level and duration of Ca^{2+} influx through NMDARs can differentially activate Ca^{2+} the Ca^{2+}-mediated kinase, CaMKII, known to promote long term potentiation (LTP), or the Ca^{2+}-mediated phosphatase, calcineurin, which is associated with long-term depression (LTD).[15,16] These two Ca^{2+}-binding proteins antagonistically control the shape, number, and size of the spines.[15,16] The fact that the ER was shown to differentially distribute in mushroom-shaped spines alludes to the formation of ER-PM junctions at mature synapses.[12]

ER-PM junctions are essential membrane hubs with two primary roles: they regulate Ca^{2+} flux, mostly in response to changes in ER Ca^{2+} levels, and they mediate membrane remodeling by transferring/shuttling lipids between the ER and the PM.[20–22] Canonical protein-protein interactions at ER-PM junctions are those between the ER-resident Ca^{2+} sensor, stromal-interaction molecule (STIM), and the PM-localized Ca^{2+} channel, ORAI, which promotes Ca^{2+} influx via the store-operated Ca^{2+}-entry pathway, following Ca^{2+} release from the ER.[23,24] Other protein constituents of the ER-PM junctions, some of which are *bona fide* molecular tethers, include the vesicle-associated membrane protein-associated proteins (VAPs), phospholipid- and glycerolipid-binding/transport proteins, Ca^{2+} sensors, ion channels/receptors, and other membrane proteins that together define the cellular processes that occur within these microdomains.[9,20,21] Equally relevant are the lipid components of ER-PM junctions, i.e., phospholipids/phosphoinositides (PIs), cholesterol, sphingomyelin, and glycosphingolipids (GSLs), which facilitate the recruitment of specific proteins or protein complexes and modulate their localized activities.[9,22,25,26] It has been proposed that, in neurons, ER-resident PIs are transported to the PM by transmembrane protein 24 (TMEM24), which re-localizes from the ER to the ER-PM junctions in response to Ca^{2+} signaling.[27,28] At this location, PIs are converted into phosphatidylinositol-4-phosphate (PIP) and phosphatidylinositol 4,5-bisphosphate (PIP2) signaling molecules by membrane-bound neuronal phosphatases and kinases.[29,30] Altering the lipid profiles of MCSs contributes to neuropathogenesis in various neurodegenerative diseases.[8,31] Until now, most studies have focused on the role of phospholipids and cholesterol at ER-PM junctions, while less attention has been given to GSLs, particularly gangliosides.[8]

Gangliosides are the most prominent sialo-glycolipids in the mammalian brain.[32] The levels and subcellular distribution of gangliosides change in a regulated, region-specific manner during basic neuronal processes.[33] Maintaining their homeostatic concentration ensures the integrity and proper composition of neuronal membranes. Among the complex gangliosides, the monosialylated GM1 is the most abundant.[34] Because of its amphiphilic structure, GM1 can engage in hydrophobic and hydrophilic interactions with membrane receptors, ion (Ca^{2+}) channels/transporters, or other extracellular ligands.[34,35] In addition, GM1 can cluster transiently within the bilayer and help form and stabilize membrane subdomains, such as the lipid rafts or glycosphingolipid-enriched microdomains (GEMs), which are structural constituents of MCSs.[35–38] Within these membrane microdomains, GM1 has both signaling and regulatory functions that depend on its ability to modulate intracellular Ca^{2+} levels by directly binding Ca^{2+} ions or interacting with Ca^{2+} channels/pumps/transporters and/or Ca^{2+}-binding proteins/receptors.[34,39,40] In neurons, changes in GM1 levels are coupled to fluctuations in intracellular Ca^{2+}, affecting neuritogenesis, spine formation, LTP, LTD, and synaptic activity.[34,35] During neuritogenesis, GM1 stimulates neurite formation by interacting with the active, phosphorylated forms of the neurotrophic receptors, tropomyosin receptor kinase (TrkA, B, and C). Moreover, exogenous GM1 was shown to increase the levels of brain-derived neurotrophic factor (BDNF), the cognate ligand of TrkB.[41,42]

Catabolism of GM1 occurs in lysosomes and is solely mediated by the lysosomal enzyme β-galactosidase (β-GAL).[43,44] Genetic mutations resulting in deficient β-GAL activity cause GM1-gangliosidosis, a severe neurodegenerative lysosomal storage disease, affecting children, adolescents, and adults.[43,44] The neuropathologic course of GM1-gangliosidosis has been largely attributed to deregulation of cellular pathways triggered by the accumulation of GM1 in neurons.[43,44] These features are replicated in *β-Gal*$^{-/-}$ mice that develop severe neurologic abnormalities early in life (i.e., tremor, ataxia, and paralysis of the hind limbs) that are accompanied by accumulation of GM1 in neurons of the brain and spinal cord, leading to massive cell death and neuroinflammation.[45,46] At the molecular level, we have shown that GM1 accumulates in the GEM fraction of the mitochondria-associated ER membranes (MAMs), where it binds to the phosphorylated/active form of the ER-resident inositol trisphosphate receptor (IP3R-1) Ca^{2+} channel, driving Ca^{2+} efflux from the ER into the mitochondria through a tethering Ca^{2+} megapore.[36] This elicits the simultaneous activation of the unfolded protein response and mitochondria-mediated apoptosis.[36,47] However, the pathogenic consequences of altered GM1 concentration at the PM, where the ganglioside normally resides, have not been explored.

Here, we show that GM1 not only is an integral component of ER-PM junctions but also favors the tethering of the apposed membranes. Increased levels of GM1 in *β-Gal*$^{-/-}$ neurons is accompanied by increased formation of ER-PM junctions, which affect overall synaptic architecture. We propose a mechanism by which active phosphorylated NMDARs (pNMDARs) are retained at *β-Gal*$^{-/-}$ ER-PM junctions by interaction with GM1. This, in turn, activates Ca^{2+}-mediated extracellular signal-regulated kinase (ERK) signaling, thereby increasing dendritic spine formation without affecting synaptic density.

RESULTS

β-Gal$^{-/-}$ Purkinje cells have increased formation of ER-PM junctions

To investigate the effects of GM1 accumulation on the formation, number, and structural features of ER-PM junctions, we first visualized these MCSs at the ultrastructural level by using transmission electron microscopy (TEM). We analyzed Purkinje cells because of their large cell bodies and extensive pathology in *β-Gal*$^{-/-}$ mice, as previously reported.[45,48] Morphologic comparison of wild-type (WT) and *β-Gal*$^{-/-}$ Purkinje cells revealed that a high proportion of the ER membranes was juxtaposed to the PM in the *β-Gal*$^{-/-}$ cells, forming a nearly continuous network of ER-PM junctions (Figure 1A, yellow lines). Instead, in WT cells these MCSs formed much less frequently and appeared dispersed along the PM (Figure 1A, yellow lines). These ultrastructural findings were confirmed quantitatively by calculating the percentage of ER membranes occupying the perimeter of the PM in WT and *β-Gal*$^{-/-}$ Purkinje cells from 1-, 3-, and 6-month-old mice (Figure 1B). We also quantified the total number of tethering events and tethering events greater than 1 μm in length (Figures 1C and 1D). Both analyses revealed a significant increase in ER-PM junctions in the *β-Gal*$^{-/-}$ Purkinje cells compared to WT cells (Figures 1B–1D). In addition, the number of tethering events greater than 1 μm was significantly higher in the *β-Gal*$^{-/-}$ Purkinje cells from 1- and 6-month-old *β-Gal*$^{-/-}$ mice, giving the appearance of continuous ER juxtaposition to the PM (Figure 1A, black box). These results suggest that high concentration of GM1 favored the formation of ER-PM junctions.

In both WT and *β-Gal*$^{-/-}$ Purkinje cells, the distance between the apposing membranes was <35 nm (Figure S1A), as previously reported in other cell types.[2,3] Occasionally, however, portions of the ER cisternae involved in junction formation narrowed into high-density regions, usually predictive of high protein content, where the ER lumen collapsed and the space between the ER membranes and the juxtaposed PM was no longer visible (Figure S1B). However, no significant difference in the number of these ER-PM junction densities was observed in WT and *β-Gal*$^{-/-}$ Purkinje cells from mice of different ages (Figure S1C). These electron-dense regions were also observed in unusual triple-contact sites that appear to form between the ER-PM junctions and the MAMs (Figures S1D and S1E). These triple MCSs were significantly higher in number in the *β-Gal*$^{-/-}$ Purkinje cells, compared to the WT cells (Figure S1F), a finding that aligns with a significant increase in the number of MAMs (Figures S1G and S1H), as previously reported.[36]

Another feature characteristic of the ER-PM junctions was the repositioning of ribosomes that appeared excluded from the face of the cisternae closest to the PM, thereby enabling a tighter association between the apposing membranes[12] (Figure S1A). The overall increase in ER-PM junctions in *β-Gal*$^{-/-}$ Purkinje cells suggests changes in the cellular pathways that control the formation of these MCSs.

Exogenous supplementation of GM1 promotes the formation ER-PM junctions in WT cells

We next tested whether the increased number of ER-PM junctions was directly linked to GM1 accumulation at the respective membranes. We used HeLa cells exogenously loaded with GM1 and transduced with the GFP-expressing construct membrane-attached peripheral

ER (MAPPER),[49] which selectively detects the formation of ER-PM junctions in real time along the PM surface. At baseline, GFP^+ puncta could be visualized along the cell surface in response to GM1 loading, while they were hardly detectable in untreated cells (Figure 2A and insets). To facilitate the quantification of the fluorescent GFP^+ puncta, we further enhanced the changes in fluorescent intensity from baseline by inducing ER Ca^{2+} depletion and, in turn, ER-PM junction formation with thapsigargin. Live-cell imaging of untreated and GM1-loaded HeLa cells for up to 10 min revealed a significant increase in GFP^+ fluorescence signal from baseline in response to thapsigargin treatment (Figures 2A and 2B; Videos S1A and S1B): at 1.5 min, GFP^+ puncta began to build up along the PM in both untreated and treated cells, but, at 3 min, the fluorescence intensity of these puncta was significantly higher at the cell surface of GM1-loaded cells (Figures 2A and 2B; Videos S1A and S1B). At 6 min, GFP fluorescence in untreated cells returned to baseline, while GM1-loaded cells expressed GFP throughout the experiment. No response was measured after dimethylsulfoxide (DMSO) treatment (Figure 2B). These results suggest a direct response in ER-PM junction formation to the levels of GM1, potentiated by the release of Ca^{2+} from the ER.

Changes in ER dynamics following thapsigargin treatment were also monitored in non-transduced and MAPPER-transduced HeLa cells, transiently transfected with a plasmid expressing tdTomato-Calreticulin-N-16 (Figures S2A and S2B; Videos S2A, S2B, S3A, and S3B). In GM1-loaded HeLa cells, tdTomato signal increased at the PM after thapsigargin treatment, indicating increased tethering of the ER to the PM, while the tdTomato fluorescence in non-loaded HeLa cells did not overtly change (Figure S2A and insets; Videos S2A and S2B). The increase in tdTomato signal paralleled the increase in $MAPPER^+$ puncta at the PM surface (Figure S2B and insets; Videos S3A and S3B).

The formation of ER-PM junctions was also monitored in MAPPER-transduced WT and $\beta\text{-}Gal^{-/-}$ primary neurons (Figures 2C–2E). Upon transduction, $\beta\text{-}Gal^{-/-}$ neurons showed a significant increase in the total fluorescence per cell area and an overall increase in the mean fluorescence intensity (MFI) (Figures 2D and 2E). GFP^+ puncta were detected along the entire PM of the soma and neuronal projections at baseline in $\beta\text{-}Gal^{-/-}$ neurons, while, in WT neurons, a few puncta were seen in the soma and little to no $MAPPER^+$ signal was detected in the dendrites (Figure 2C and insets). These results confirm that accumulation of GM1 in $\beta\text{-}Gal^{-/-}$ neuronal membranes increases the formation of ER-PM junctions.

GM1 accumulates in the ER-PM junctions isolated from $\beta\text{-}Gal^{-/-}$ brains

To identify the proteins present at the ER-PM junctions isolated from WT and $\beta\text{-}Gal^{-/-}$ brains, we optimized a purification method that enabled the enrichment of fractions containing ER, PM, and ER-PM junctions (Figure S3A and S3B). These fractions were tested for purity on immunoblots probed with the ER and PM markers, calnexin and N-cadherin, respectively (Figure 3A). Proteins that populate ER-PM junctions, such as ORAI1, STIM1, STIM2, and VAP A and B isoforms (VAPA/B), were enriched in both WT and $\beta\text{-}Gal^{-/-}$ fractions, but their levels were similar in both set of samples, indicating that they were not affected by GM1 accumulation (Figure 3A). Moreover, using HRP-conjugated cholera toxin B subunit (CTX-B), which selectively binds GM1, we detected a massive

accumulation of the ganglioside in all three β-*Gal*$^{-/-}$ fractions, but especially in the ER-PM junctions (Figure 3A). These results were further corroborated by high-performance thin-layer chromatography (HPTLC) assays (Figures 3B and 3C). The levels of GM1 were so high in the β-*Gal*$^{-/-}$ fractions that we needed to increase the concentration of the WT fractions by 3-fold to detect a signal. Band quantifications, after normalization to loading, from eight independent experiments revealed that the highest GM1 levels were in the ER-PM junction fractions from WT and β-*Gal*$^{-/-}$ brains, indicating that GM1 is a normal constituent of these MCSs (Figure 3C). However, the amount of GM1 in the β-*Gal*$^{-/-}$ ER-PM junctions was almost 10 times greater than that in WT controls (Figure 3C).

Although the weights of the WT and β-*Gal*$^{-/-}$ brains were comparable at the start of the purification procedure, the fraction comprising the ER-PM junctions from the β-*Gal*$^{-/-}$ brains consistently contained a higher protein content than did the corresponding WT fraction (Figure S3C), further supporting the notion that β-*Gal*$^{-/-}$ neurons have more ER-PM junctions. Using HPTLC, we monitored how GM1 levels changed in ER-PM junctions during disease progression compared to the WT fractions (Figures 3D and 3E). GM1 bands were quantified in four independent assays (Figure 3E). The β-*Gal*$^{-/-}$ ER-PM junctions showed progressive accumulation of GM1 as the animals aged, with significantly higher levels of the ganglioside, compared to that in the WT fractions, starting at 3 months of age (Figures 3D and 3E). GM1 levels in WT ER-PM junctions remained similar at all ages, suggesting that GM1 gradually clusters at these MCSs only during disease progression. This was even more evident in the GEM fractions isolated from purified β-*Gal*$^{-/-}$ ER-PM junctions, which contained the highest levels of GM1 (Figure S3D). GEM purity was assessed by using the caveolae marker, flotillin 1, which was higher in the GEMs of both WT β-*Gal*$^{-/-}$ compared to all other fractions (Figure S3D).

Comparative proteomic analysis of β-*Gal*$^{-/-}$ ER-PM junctions predicts upregulation of the synaptogenesis-signaling pathway

We next employed a label-free, spectral-count comparative proteomic analysis to examine which proteins were differentially expressed in the ER-PM junctions isolated from WT and β-*Gal*$^{-/-}$ brains. The variance between the samples was low, and a total of 2,212 proteins were identified (ProteomeXChange: PXD042994), most of which resided in the ER/cytoplasm (1,288), and the PM (513) (Figure S4A). Many of the identified proteins belonged to major families of kinases, proteases, enzymes, transporters, ion channels, and G-protein-coupled receptors (ProteomeXChange: PXD042994). Although many of the differences did not reach significance, the fold changes highlighted a trend of upregulation for some of the molecules that were then validated by immunoblot analysis. Notably, among the upregulated proteins in the β-*Gal*$^{-/-}$ samples were *bona fide* components of the ER-PM junctions, including ORAI2 and TMEM24 (Figure S4B).

The ER Ca^{2+}-release channels IP3R-3 and ryanodine receptor types 2 and 3 (RYR2 and RYR3) were also increased, with RYR2 showing a significant change (Figure S4B). These results conform with the deregulated activity of the pIP3R-1 seen in the β-*Gal*$^{-/-}$ MAMs.[36] Other proteins of interest that were differentially expressed in β-*Gal*$^{-/-}$ ER-PM junctions were the glutamate ionotropic receptor NMDAR type 1 subunit, which increased 10-fold,

and TrkB, which increased 1.6-fold, although the fold changes in levels for both proteins did not reach significance (Figure S4B). Both receptors are associated with LTP and promote postsynaptic spine formation by activating the mitogen-activated protein kinase (MAPK)/ERK signaling pathway.[41,50] We found that both ERK1 (also called MAPK3; 1.5-fold increase) and ERK2 (also called MAPK1; 1.3-fold increase) showed an upward trend in the *β-Gal*$^{-/-}$ samples (Figure S4B). In addition, the membrane-bound kinases, phosphatidylinositol 4-kinase type 2A (PI4K2A) and phosphatidylinositol-4-phosphate 5-kinase type 1C (PIP5K1C), which phosphorylate PIs, showed some of the highest predicted fold increases (Figure S4B).

We further validated some of the proteins upregulated in the *β-Gal*$^{-/-}$ ER-PM junctions on immunoblots and quantified them by comparing WT and *β-Gal*$^{-/-}$ fractions (Figures 4A–4F and S4C–S4F). The levels of NMDAR type 1 subunit, TMEM24, PI4K, PIP5K1, and TRKB were significantly higher in the *β-Gal*$^{-/-}$ ER-PM junctions (Figures 4A–4F). Given that the activated form of NMDAR type 1 subunit, which is phosphorylated at Ser896 (pNMDAR), traffics the receptor to the PM and accumulates at the synapses,[51] we also tested its levels and found it to be significantly increased in *β-Gal*$^{-/-}$ ER-PM junctions (Figures 4A and S4C). Although ERK1/2 levels did not differ between WT and *β-Gal*$^{-/-}$ fractions, the active phosphorylated forms of ERK1/2 (pERK1/2) were significantly increased in the *β-Gal*$^{-/-}$ ER-PM junctions (Figure 4E). Moreover, the increased ratio of pERK/ERK inferred enhanced ERK signaling at these MCSs (Figure S4D). We found that BDNF, the cognate ligand of TRKB, which increases NMDAR activity and Ca^{2+} influx through NMDAR,[52,53] was also significantly upregulated in the *β-Gal*$^{-/-}$ samples (Figure 4F). Regarding PI4K, antibody against this protein binds to two isoforms with different molecular weight: the 230-kDa isoform (Figures S4E and S4F) is mostly associated with the ER, while the 55-kDa isoform (Figure 4C) resides at the PM. Interestingly, we found that only the PM-localized 55-kDa isoform was significantly increased in the *β-Gal*$^{-/-}$ fractions (Figure 4C).[54,55]

We next uploaded the proteomics data to the Ingenuity Pathway Analysis (IPA) software to identify cellular pathways potentially dysregulated in the *β-Gal*$^{-/-}$ ER-PM junctions. The top canonical pathways above a threshold of 0.05, according to the Fischer's exact test *p* value, were graphed, and a *Z* score was used to predict whether the pathways were activated (positive *Z* score, orange) or inhibited (negative *Z* score, blue), based on the differentially expressed proteins (Figure 4G). The most upregulated was the synaptogenesis-signaling pathway. Targets for both the presynaptic and postsynaptic terminals were present in our proteomic data, reiterating a role for ER-PM junctions at synapses (ProteomeChange: PXD042994). In addition, the synaptic LTP pathway was predicted to be highly upregulated (Figure 4G). This pathway is mostly associated with increased protein expression at the post-synapse, leading to increased connectivity.[16]

We next generated a network map of the proteins involved in the synaptogenesis-signaling pathway that were found dysregulated in the proteomics of *β-Gal*$^{-/-}$ ER-PM junctions (Figure 4H). This signaling pathway includes several neuronal processes, such as scaffolding of the postsynaptic density, synaptic vesicle binding, neurite outgrowth, and synapse stabilization, all of which are regulated by ERK1/2 activation downstream of NMDAR and TRKB (NTRK2) signaling.[50,56,57] All these processes were predicted to be upregulated in

the *β-Gal*$^{-/-}$ ER-PM junctions (Figure 4H). We also identified increased Ca^{2+} release from the ER, which concurs with previous findings in our mouse model (Figure 4H).[36] Together, these results suggest that GM1 accumulation at *β-Gal*$^{-/-}$ ER-PM junctions disturbs synaptic architecture and function, especially at the post-synapse.

GM1 accumulation in *β-Gal*$^{-/-}$ neurons affects the morphology of the dendritic arbor and increases spine formation

To better understand how GM1 accumulation affects the post-synapse, we employed Golgi-Cox staining of the cortex, hippocampus, and cerebellum from 6-month-old WT mice and *β-Gal*$^{-/-}$ mice. The number of dendrites in the *β-Gal*$^{-/-}$ brain was lower than that in the WT brain; this reduction was prominent in the cellular layers of the cortex, the *cornus ammonis* (CA) of the hippocampus, and the deep cerebellar nucleus (Figure S5A).

The cortical neurons of *β-Gal*$^{-/-}$ mice contained dendritic structures not found in WT controls, including numerous aberrant neurite outgrowths or ectopic dendrites at the beginning of the dendritic arbor (Figure S5B). Another morphologic abnormality was the formation of dendritic beading (Figure S5C). This unusual “string of beads” along the dendrites denotes dendritic swelling.[58] The latter often follows dendritic injury and is associated with improper trafficking of molecules between the neuronal cell body and the dendrites, leading to a “traffic jam” along the branch and resulting in a bulge.[59] In addition, these neurons had retracted processes and little branching, indicative of an unhealthy neuronal state most likely preceding apoptosis (Figure S5C).

Next, we investigated whether GM1 accumulation in the *β-Gal*$^{-/-}$ neuronal membranes and ER-PM junctions would affect the number and morphology of dendritic spines. These structures were easily recognized in the pyramidal neurons of the cortex (Figure S5D) and hippocampus (Figures 5A and S5E). For quantification, we focused on hippocampal pyramidal neurons because that region is involved in LTP, a process that was predicted to be upregulated in the proteomics of *β-Gal*$^{-/-}$ ER-PM junctions (Figure 4G). In the *β-Gal*$^{-/-}$ dendritic branches stained by Golgi-Cox, the number and density of the spines were visibly increased (Figures 5A and S5E). For comparative quantification of the number of spines, we used Imaris Imaging software’s semiautomated filament tracer to obtain three-dimensional (3D) reconstructions of z-stacked images of Golgi-Cox-stained pyramidal neurons from the CA2 region of WT and *β-Gal*$^{-/-}$ hippocampi (Figures 5B and 5C). Quantification of the number of spines within a 10-μm length of dendrite revealed a significant increase in spine density in the *β-Gal*$^{-/-}$ pyramidal neurons, compared to that in the WT samples (Figure 5C). The number of spines in WT neurons concurred with what has been reported using immunofluorescence imaging,[60,61] thus supporting the validity of this method for spine-density quantification. These results suggest that GM1 accumulation at the ER-PM junctions favors spine formation.

Increased number of dendritic spines in the *β-Gal*$^{-/-}$ brain does not result in increased synaptic density

An increased number of dendritic spines usually precedes synapse formation.[62] Therefore, we ascertained whether the increased spine density in *β-Gal*$^{-/-}$ dendrites would increase

the number of synaptic connections. In TEM images, the spines and dendritic branches were readily discernible as cross-sectioned, circular structures within the extensive dendritic arborizations of the CA2 hippocampal pyramidal neurons and cerebellar Purkinje cells (Figures 5D and S6A). These structures were visibly more numerous in the *β-Gal*$^{-/-}$ brain, further confirming the increased formation of spines, albeit their membranes appeared fuzzy and less defined, possibly due to GM1 accumulation (Figures 5D and S6A). Surprisingly, however, the increased number of spines did not correlate with increased synaptic connections, as determined by the significantly reduced number of electron-dense regions, known as synaptic densities, in the *β-Gal*$^{-/-}$ brain (Figures 5D, 5E, S6A, and S6B).

These results would indicate that, in the *β-Gal*$^{-/-}$ brain, there is an increase in the number of post-synapses (spines) without a corresponding increase in the number of pre-synapses (axons). We confirmed this assumption by looking at the levels of the postsynaptic marker, postsynaptic density marker protein 95 (PSD-95), and the presynaptic marker synaptophysin 1 (Syp1) in the hippocampus and cerebellum of WT and *β-Gal*$^{-/-}$ brains (Figures S6C and S6D). In *β-Gal*$^{-/-}$ hippocampal sections, we detected a significant increase in the fluorescent levels of PSD-95 in the CA2 region, while Syp1 was significantly decreased (Figures S6E and S6F). In the *β-Gal*$^{-/-}$ cerebellum, fluorescent levels of PSD-95 were significantly increased, while Syp1 was similar between WT and *β-Gal*$^{-/-}$ cerebellar lobules (Figures S6E and S6F).The increase in postsynaptic staining was also confirmed by immunoblot analysis of tissue lysates from total cerebella and hippocampi isolated from WT and *β-Gal*$^{-/-}$ mice, which showed a significant increase in PSD-95 levels with no changes in the levels of Syp1 (Figures S6G–S6I), suggesting that the decreased presynaptic staining and degree of synaptic connectivity, specifically in the hippocampus, varies by region.

GM1 binds pNMDAR and maintains it in an activated state

The observed increase in the levels of total NMDAR type 1 subunit and pNMDAR in the *β-Gal*$^{-/-}$ ER-PM junctions suggested hyperactivation of the receptor at these MCSs. To link these changes in NMDAR levels to the accumulation of GM1 at the ER-PM junctions, we tested whether GM1 interacts with NMDAR type 1 subunit at these MCSs. Co-immunoprecipitation (coIP) experiments were performed on the GEM fractions of the ER-PM junctions isolated from WT and *β-Gal*$^{-/-}$ brains. Using antibodies against pNMDAR (Ser896) and NMDAR type 1 subunit, we co-immunoprecipitated GM1, demonstrating a specific interaction between these molecules within the ER-PM junctions (Figures S7A and S7B).

In the reverse reaction, we used biotinylated CTX-B to pull down GM1 and found that active pNMDAR preferentially interacted with the ganglioside in the *β-Gal*$^{-/-}$ GEMs (Figure 6A). In contrast, the non-phosphorylated NMDAR type 1 subunit appeared to bind GM1 with higher affinity in the WT GEMs (Figure 6A). Quantitatively, the ratio of pNMDAR to NMDAR was significantly higher in the GEMs from the *β-Gal*$^{-/-}$ ER-PM junctions than in the corresponding WT fractions (Figure 6B). Levels of NMDAR and pNMDAR were also measured by immunoblot in the purified ER and PM fractions to determine whether the ER-PM junctions were the main contributor to increased NMDAR levels. In these fractions,

NMDAR and pNMDAR levels were not significantly different between WT and *β-Gal*$^{-/-}$ fractions, while both were increased in the ER-PM junction fractions (Figures S7C–S7E).

The physical interaction between these molecules was further validated by co-staining primary neurons isolated from WT and *β-Gal*$^{-/-}$ brains with NMDAR type 1 subunit antibody and Alexa Fluor 555-conjugated CTX-B. NMDAR was increased in *β-Gal*$^{-/-}$ neurons, and its distribution pattern overlapped with that of CTX-B, indicating a high degree of co-localization between these molecules (Figure 6C). Although the levels of NMDAR and GM1 were quite low in the WT cells, we still detected their co-localization, supporting the notion that these molecules interact under physiological conditions (Figure 6C). Together, these results demonstrate that GM1 clusters active pNMDAR in the cellular locations where the ganglioside accumulates. We can predict that GM1-mediated clustering of NMDAR at the synapses may evoke Ca^{2+} signals, although future electrophysiology studies will be needed to support this notion.

GM1 buildup at the ER-PM junctions of *β-gal*$^{-/-}$ neurons affects Ca^{2+} homeostasis and increases the level of calcineurin

The main function of NMDARs is to regulate Ca^{2+} influx into neurons by glutamate stimulation, thereby modulating neuroplasticity.[16] In contrast, GM1 modulates Ca^{2+} flux through its capacity to bind Ca^{2+} and influence the activity of Ca^{2+}-binding proteins/receptors.[34,36] Thus, we hypothesized that GM1 accumulation at the ER-PM junctions and its interaction with pNMDARs at the GEMs provokes a rise in cytosolic Ca^{2+} levels. To test this hypothesis, we measured the cytosolic levels of Ca^{2+} in primary neurons from WT and *β-Gal*$^{-/-}$ brains transduced with a lentivirus expressing GCamp6s, a genetically encoded fluorescent Ca^{2+} indicator. Quantification of the intensity of GCamp6s fluorescence revealed a significantly higher level of Ca^{2+} in *β-Gal*$^{-/-}$ primary neurons than in WT controls (Figures 7A and 7B). To link this phenomenon directly to GM1 concentration, we used HeLa cells transduced with GCamp6s that were exogenously loaded with GM1. These cells showed a significantly higher level of GCamp6s fluorescence than did untreated cells (Figure S8A and S8B). Because many Ca^{2+}-dependent neuronal processes at synapses induced by NMDAR-mediated Ca^{2+} influx are modulated by the activities of CaMKII and calcineurin, we also tested the levels of these proteins in *β-Gal*$^{-/-}$ ER-PM junctions (Figures 7C and 7D). In the *β-Gal*$^{-/-}$ ER-PM junctions, we found that calcineurin A was significantly upregulated while CaMKII was unchanged (Figures 7C and 7D), suggesting a role of calcineurin A at these MCSs in the regulation of plasticity in response to the increased number of spines.

DISCUSSION

In this study, we addressed the role of the sialoglycosphingolipid GM1 in Ca^{2+}-mediated processes, where it acts as an integral constituent of the ER-PM junctions. Under neuropathologic conditions that ensue downstream of genetic deficiency of the lysosomal enzyme β-Gal, chronic buildup of GM1 within these MCSs alters the properties of their lipid and protein components, ultimately leading to a synaptopathy associated with abnormal *de novo* spine formation and altered intracellular Ca^{2+} levels.

The NMDAR Ca^{2+} channel is highly expressed in excitatory post-synapses, where it promotes LTP and spine formation, especially in the pyramidal cells of the hippocampus.[16,65] In addition, NMDAR-induced Ca^{2+} influx into the cytosol of neurons influences the localization of the lipid transporter TMEM24 to the ER-PM junctions.[28] TMEM24 has been shown to function as a PI transporter in pancreatic β cells.[27] Although this function of TMEM24 has not yet been demonstrated in neurons, it is possible that this molecule relocates to the *β-Gal*$^{-/-}$ ER-PM junctions, thereby facilitating the transport of PIs to these MCSs during synaptogenesis and spine formation. This hypothesis would explain why we detect increased levels of PI4K and PIP5K1 that convert PIs within the MCSs into PIP and PIP2, both of which are potent neuronal-signaling molecules that modulate the activity and PM expression of NMDARs at the synapse[63] (Figure 7E). Further studies are needed to corroborate this hypothesis.

One important function of GM1 is to interact with phosphorylated membrane receptors, thereby prolonging their activation. We found that GM1 interacts specifically with pNMDARs phosphorylated at Ser896, a site that increases the receptor's expression at the PM and holds this Ca^{2+} channel in an active conformation at the ER-PM junctions. This interaction may alter Ca^{2+} influx, leading to excessive spine formation downstream of ERK without increasing connectivity to the presynaptic axons (Figure 7E). These results parallel what we have previously shown in the MAMs, where GM1 binds pIP3R-1 in an active phosphorylated state, increasing ER Ca^{2+} efflux through the pIP3R-1/VDAC1/GRP75 Ca^{2+} megapore.[36] In addition, binding GM1 to phosphorylated, active TrkB at the PM favors its interaction with BDNF, which, in turn, induces neuritogenesis, again downstream of ERK signaling.[41] BDNF also contributes to the maturation of synaptic spines in the hippocampus and increases their numbers[56]; both of these processes may potentiate the effects of NMDARs.

The increase in both NMDAR and intracellular Ca^{2+} suggests that LTP is induced in the *β-Gal*$^{-/-}$ mice, a process known to enhance postsynaptic spine density. However, we found that the increase in intracellular Ca^{2+} levels activates calcineurin rather than CaMKII within the ER-PM junctions. Calcineurin is normally associated with LTD not LTP, which is instead downstream of CaMKII. In neurons, calcineurin dampens intracellular Ca^{2+} levels by dephosphorylating and inactivating voltage-gated Ca^{2+} channels at the PM,[66] which eventually decreases synaptic spine density.[67,68] On the other hand, calcineurin is also known to modulate ERK signaling at the PM by interacting with and dephosphorylating the kinase suppressor of Ras 2 (KSR2), thereby influencing KSR2 localization and ERK-scaffold activity in response to Ca^{2+} signals. This, in turn, promotes BDNF production and ultimately contributes to the increased number of spines,[69] as seen in our *β-Gal*$^{-/-}$ model. A potential explanation for these opposite roles of calcineurin in spine formation is that high levels of the phosphatase specifically at the ER-PM junctions may counteract the increase in the number of non-connecting spines, thereby promoting LTD. However, chronic activation of pNMDARs in complex with GM1 at ER-PM junctions may outcompete calcineurin's capacity to limit the number of spines. Further studies will be required to dissect the role of calcineurin in the regulation of synaptic plasticity at the ER-PM junctions.

Altered numbers of synaptic spines have been reported in several neurologic conditions, including common neurodegenerative diseases, autism spectrum disorders, and fragile X syndrome.[70–72] In fragile X syndrome, the combined deregulation of metabotropic glutamate receptors and increased sensitivity to BDNF signaling contribute to excessive dendritic branching and spine formation.[70,71] These findings further support the idea that increased NMDARs and BDNF most likely cause excessive spine formation in *β-Gal*$^{-/-}$ mice.

A common element that adds to the complexity of MCS-regulated pathways is altered Ca^{2+} signaling caused by GM1 accumulation at both the MAMs and ER-PM junctions, two MCSs with similar structural and functional characteristics. Interestingly, we observed an increased number of triple-contact sites involving the ER, PM, and mitochondria in *β-Gal*$^{-/-}$ neurons compared to WT neurons. These sites may bridge the activity of the MAMs and ER-PM junctions, potentiating the effects of increased Ca^{2+} concentration at the synapses of the *β-Gal*$^{-/-}$ mice.

Given that β-Gal-mediated catabolism of GM1 occurs in lysosomes and that these organelles tether/fuse with virtually all other intracellular membranes and the PM, understanding the effects of GM1 accumulation at MCSs involving the lysosomal membrane warrants further investigation.

Limitations of the study

1. TEM analyses of MAPPER+ HeLa cells, with and without GM1 loading, to detect ER-PM junction formation would further corroborate the MAPPER immunofluorescence data. However, at the ultrastructural levels, HeLa cells showed a highly heterogeneous morphology of their PM that varied depending on the level of optical sectioning. This caveat made the visualization and accurate quantification difficult. Moreover, TEM images would only allow a subsampling of ~50 nm, while the z resolution of confocal images shown in Figure 2 spanned over 670 nm, allowing for a larger sampling size to readily detect ER-PM junction formation.
2. Neuronal electrophysiology studies would be needed to fully dissect the implications of increased NMDAR levels on LTP and neuronal signaling at the synapse. Patch clamp experiments, paired with specific Ca^{2+} channel blockers, would also provide a more sensitive approach to elucidate the source of intracellular Ca^{2+} levels in the *β-Gal*$^{-/-}$ neurons. However, our lab is not equipped to perform these experiments that require specific expertise and equipment.

STAR★METHODS

Detailed methods are provided in the online version of this paper and include the following:

RESOURCE AVAILABILITY

Lead contact—Further information and requests for resources and reagents should be directed to and will be fulfilled by the lead contact, Alessandra d'Azzo (Sandra.dAzzo@stjude.org).

Materials availability—Plasmids used in this study are readily available at Addgene. This study did not generate new unique reagents.

Data and code availability

- Proteomics data have been deposited to the ProteomeXchange Consortium via the PRIDE partner repository with the dataset identifier (ProteomeXChange: PXD042994) and are publicly available as of the date of publication. Accession numbers are listed in the key resources table. All other data is available to be shared by the lead contact upon request.
- No original code has been generated for this study.
- Any additional information required to reanalyze the data reported in this paper is available from the lead contact upon request.

EXPERIMENTAL MODEL AND SUBJECT DETAILS

Animal model—Animals were housed in a fully AAALAC (Assessment and Accreditation of Laboratory Animal Care)-accredited animal facility with controlled temperature (22°C), humidity, and lighting (alternating 12–h light/dark cycles). Food and water were provided *ad libitum*. All procedures in mice were performed according to animal protocols approved by the St. Jude Children's Research Hospital Institutional Animal Care and Use Committee (IACUC) and NIH guidelines. The β-*Gal*$^{-/-}$ murine model was generated to ablate a functional β-*Gal* gene[45]. WT and β-*Gal*$^{-/-}$ mice (C57BL/6J background), aged 5 days (p5) to 6 months, were used for experiments and are described in the method details. Both male and female mice were used in all experiments without any apparent sex differences.

Cell lines—HeLa cells and HEK293T cells were maintained in culture in Dulbecco's Modified Eagles Medium (DMEM, Gibco) supplemented with penicillin/streptomycin (100 µg/mL) (Gibco), 2 mM GlutaMAX (Gibco), and 10% fetal bovine serum (FBS; Thermo Fisher) and incubated at 37°C in 5% CO_2.

Primary neurons were isolated from WT and β-*Gal*$^{-/-}$ mice (as described in method details), plated on poly-D-lysine–coated glass coverslips, cultured in MACS Neuro Medium (Miltenyi) containing MACS NeuroBrew-21 (Miltenyi), and incubated at 37°C in 5% CO_2.

METHOD DETAILS

Transmission electron microscopy analysis—Mouse brains were isolated and fixed in 0.1M cacodylate buffer containing 2.5% glutaraldehyde and 2% paraformaldehyde (PFA). Fixed brains were embedded in 4% low–melting point agarose (Sigma Aldrich) and cut into 100-µm sagittal sections on a VT1000 S vibratome (Leica). Samples were postfixed in reduced osmium tetroxide and contrasted with aqueous uranyl acetate. Dehydration

was performed by a series of ethanol baths, ascending in concentration from 70% to 100%, followed by 100% propylene oxide. Samples were infiltrated with EmBed-812 and polymerized at 60°C. Embedded samples were sectioned at ~70 nm on a Leica (Wetzlar) UC-7 ultramicrotome and examined in a ThermoFisher Scientific (Hillsboro) TF20 transmission electron microscope at 80 kV. Digital micrographs were captured with an Advanced Microscopy Techniques (AMT; Woburn) imaging system. Whole-cell montages were acquired with the same AMT system controlled by serialEM software.[76] Montages were stitched and exported as.tiff files by using IMOD software.[75] Unless otherwise indicated, all reagents were from Electron Microscopy Sciences (Hatfield). For ER-PM junction quantification, Purkinje cell bodies were imaged by montage around the entire soma. The total length of the PM and the fragments of ER within 35 nm of the PM were traced and measured. To quantify synaptic density, 3 consecutive images were taken of the dendritic arbor of Purkinje cells, and the average numbers of synaptic densities per area were measured. In the hippocampus, consecutive images were taken of the dendritic arbors parallel to the pyramidal cell layer in the CA2 region to determine the average number of synaptic densities per area.

Production of lentivirus vector—Lentiviral vector preparations were produced by co-transfection of HEK293T cells with a mixture of 4 plasmids (13.5 μg pCAG-kGP1–1R, 4.5 μg pCAG4-RTR2,[77] 4.5 μg envelope plasmid pCAG-VSVG, and 22.5 μg vector plasmid pCL20-GFP-MAPPER or pGP-CMV-GCaMP6s) using the calcium phosphate precipitation method: 9×10^6 HEK293T cells were seeded onto 15-cm tissue culture dishes 24 h before transfection. The mixture of plasmids was diluted to a total volume of 450 μL with ddH_2O. Then 50 μL 2.5M $CaCl_2$ was added, and the mixture was incubated for 5 min at room temperature (RT); 2× Hank's balanced salt solution (HBSS; 500 μL) (50mM HEPES, pH 7.05; 280mM NaCl, 1.5mM Na_2PO_4) was added dropwise while vortexing, and the mixture was incubated for 10 min at RT. The final mixture (1 mL DNA-$CaPO_4$-HBSS) was added dropwise to a 15-cm dish containing 25 mL DMEM supplemented with penicillin/streptomycin (100 μg/mL), 2 mM GlutaMAX, and 10% FBS and then mixed well by swirling/tilting the dish.

The cells were incubated at 37°C in 5% CO_2 for 18 h. The medium was exchanged for Neurobasal medium [−] L-glutamine (Gibco, Cat. No. 21103–049) without serum, and the cells were incubated for 24 h. The next day, the supernatant containing virus was collected, cleared by 500 ×*g* for 5 min at RT and filtered through a 0.45-μm filter. The virus was concentrated (~100×) by ultracentrifugation at 112,400 ×*g* at 4°C for 90 min, and the viral pellet was resuspended in Neurobasal medium without serum overnight at 4°C. Aliquots were snap-frozen on dry ice and stored at −80°C.

Isolation of neurons—P5 WT mice and *β-Gal*$^{-/-}$ mice were used to set up neuronal cultures. The pups were euthanized by CO_2, and their brains were collected in dissection media (500 mL HBSS, 5 mL 1M HEPES, 6.67 mL 45% glucose, penicillin (100 U/mL), and streptomycin [100 μg/mL]). The cerebellum, olfactory bulbs, and meninges were removed and discarded. The remaining brain dissociated using the Neural Tissue Dissociation Kit – Postnatal Neurons (Miltenyi Biotec). Brains were placed in a gentleMACS C tube (Miltenyi

Biotec) with the supplied enzymes and dissociated on a gentleMACS Octo Dissociator with Heaters (Miltenyi Biotec) on the "NTDK_37C″ program. The brain suspension was passed through a 1000-μL pipette tip 5× with 1mL of 5% bovine serum albumin (BSA)/PBS to fully homogenize it and filtered on a 70μm cell strainer. Tubes were centrifuged at 300 ×*g* for 5 min, and the supernatant was removed. The pellet was resuspended in 80 μL cold 5% BSA/PBS and 20 μL non-neuronal cell biotin antibody (Miltenyi Biotec; Neuron Isolation kit) and incubated at 4°C for 5 min. The pellet was resuspended in 800 μL cold 5% BSA passed through an LS column (Miltenyi Biotec) on a magnetic strip to remove non-neuronal cells. The flow through, which contained the neurons, was collected and centrifuged at 300 ×g for 5 min at 4°C. Mixed neuronal cells were plated in poly-D-lysine–coated 2-well glass coverslip chambers (LabTak) using MACS Neuro Medium (Miltenyi) containing MACS NeuroBrew-21 (Miltenyi) and incubated at 37°C in 5% CO_2.

MAPPER analysis *in vitro*—HeLa cells and primary neurons were maintained in culture in 2-well glass bottom slides (LabTek). The cells were grown until confluency and transduced with 10 μL MAPPER lentivirus in 500 μL media for 4 h at 37°C in 5% CO_2. The cells were washed 2× with PBS, fresh media was added, and the slides were incubated overnight at 37°C in 5% CO_2. For HeLa cells,1 μg/μL GM1 (Advanti) was added overnight in 0.5% serum media to load cells with GM1. Live-cell confocal imaging was performed using the Marianas 2Axio Observer microscope (Zeiss) at 37°C/5% CO_2 for 10 min in the green fluorescence channel (488 nm), capturing images every 15 s. After 1 min of imaging, 1μM thapsigargin was added to induce ER-PM junction formation, or 1μM DMSO (control) was added to the wells, and imaging was continued for 9 min. MFI was calculated using ImageJ analysis software.

Transient transfection of Calreticulin-RFP *in vitro*—MAPPER-transduced and non-transduced HeLa cells were maintained in culture in 2-well glass bottom slides (LabTek). The cells were plated at 25% confluency and transiently transfected with tdTomato-Calreticulin-N-16 (Addgene) using the Ca^{2+} phosphate transient transfection protocol as follows: 10 μg of tdTomato-Calreticulin-N-16 plasmid DNA was added to 450 μL of water and 50 μL of 2.5 M $CaCl_2$. The $CaCl_2$ solution was added dropwise to 500 μL of 2x HEPES buffered saline solution containing 0.28 M NaCl, 0.05 M HEPES (Sigma Aldrich), and 1.5 mM Na_2HPO_4, pH 7.05. The DNA/$CaCl_2$ mixtures was added to the cells dropwise and incubated overnight. Cells were washed once with PBS and fresh media was added. After 48 h, cells were imaged for 10 min, every 15 s, using live-cell confocal imaging on the Marianas 2Axio Observer microscope (Zeiss) at 37°C/5% CO_2 in the green fluorescence channel (488 nm) and red fluorescence channel (561 nm). 1μM thapsigargin was added after 1 min to monitor changes in ER morphology and ER-PM junction formation.

Isolation of ER-PM junctions—Mice were euthanized by CO_2 and total brains were isolated. Brain hemispheres were separated on ice, with each hemisphere was homogenized separately and combined prior to ER-PM-Mito enrichment steps. Brain hemispheres were homogenized in a 2-mL Kontes Dounce homogenizer (Kimble) in 1 mL homogenizer solution (0.32M sucrose, 1mM $NaHCO_3$, 1mM $MgCl_2$, 0.5mM $CaCl_2$, protease and phosphatase inhibitors) with 15 strokes of a loose-fitting glass pestle (Kimble).

Nuclear removal steps—Homogenates were transferred to a 15-mL Falcon tube and diluted up to 10% w/v (e.g., 0.225 g = 2.25 mL) with homogenizer solution and centrifuged at 1400 ×*g* for 10 min at 4°C. Supernatant was transferred to a 30-mL glass Corex tube on ice, and pellets were resuspended in the same 10% w/v homogenizer solution and homogenized in a 2-mL Kontes Dounce homogenizer with 6 strokes of a tight-fitting glass pestle (Kimble). Homogenates were transferred to a 15-mL Falcon tube and centrifuged at 710 ×*g* for 10 min at 4°C. The resulting pellet containing nuclear and cellular debris was discarded.

ER-PM-Mito enrichment steps—Supernatants were combined in a 30-mL glass Corex tube after the previous nuclear removal steps and centrifuged in a Sorvall centrifuge at 13,800 ×*g* for 10 min at 4°C. Pellets were resuspended in the same 10% w/v homogenizer solution and homogenized in a 2-mL Kontes Dounce homogenizer with 6 strokes of a tight-fitting glass pestle. Homogenates were transferred to a 30-mL glass Corex tube and centrifuged in a Sorvall centrifuge at 13,800 ×*g* for 10 min at 4°C. Homogenization and centrifugation steps were repeated, and pellets (enriched in PM, bound ER, and mitochondria [Mito]) were collected for the sequential steps. After the 3 centrifugations, supernatants were combined in a 13-mL Ultra-Clear centrifuge tube (Beckman) and ultracentrifuged in a Beckman Ultracentrifuge at 100,000 ×g for 1 h at 4°C. The resulting supernatant contained the cytosolic fraction, and the pellet contained the unbound ER fraction. Figure S2A shows representative immunoblots of the fractions collected during the nuclear removal and ER-PM-Mito–enrichment steps, probed with the appropriate organelle markers: laminin A/C (nucleus), calnexin (ER), N-cadherin (PM), lactose dehydrogenase (LDH; cytosol), and TOMM20 (mitochondria).

Sucrose gradient—The pellets (enriched in PM, bound ER, and mitochondria) were homogenized in 2 mL 11% w/v sucrose in ER-PM buffer (5 mM Bis-Tris, 0.5 mM $NaHCO_3$, 0.2 mM EDTA, protease inhibitors, pH 6) in a 2-mL Kontes Dounce homogenizer with 10 strokes of a tight-fitting glass pestle. Homogenate was layered on a discontinuous sucrose gradient containing 2 mL 53% w/v, 43% w/v, and 4 mL 38% w/v sucrose in ER-PM buffer in a 13-mL Ultra-Clear centrifuge tube and centrifuged at 100,000 ×*g* for 2.5 h at 4°C. Centrifugation resulted in 3 distinct bands: ER-PM junctions (top), mitochondria (middle), and PM (bottom). The top band was collected and resuspended in 7 mL ER-PM wash buffer (225mM mannitol, 75mM sucrose, 0.5mM EGTA, 30mM Tris-HCl, pH 7.4) and centrifuged at 13,000 ×*g* for 10 min at 4°C. Supernatant was transferred to a 13-mL Ultra-Clear centrifuge tube and centrifuged at 100,000 ×*g* for 40 min at 4°C. The resulting pellet contained the ER-PM junctions. The bottom band (PM) was collected and resuspended in 15 mL ER-PM wash buffer and centrifuged at 13,000 ×*g* for 10 min at 4°C. Supernatant was transferred to a 32-mL Ultra-Clear centrifuge tube (Beckman) and centrifuged at 48,000 ×g for 20 min at 4°C. The resulting pellet contained the PM fraction. Pellets containing ER, PM, and ER-PM junctions can be resuspended in RIPA buffer (50mM Tris-HCl, pH 7.5; 150-mM NaCl, 0.1% SDS, 1% DOC, 1% Triton X-100, protease and phosphatase inhibitors) for Western blot and proteomic analyses, in HPLC-grade water for HP-TLC analysis or separated further into the GEM fraction (see below). The bands corresponding to the ER-PM

junctions and PM fractions (Figure S2B) were individually collected and further centrifuged; the resulting pellets were then used for further experimentation.

GEM isolation of ER-PM junctions—Pellets containing ER, PM, and ER-PM junctions were resuspended in 600 μL extraction buffer (25mM HEPES, pH 7.5; 0.15M NaCl, 1% Triton X-100, and protease and phosphatase inhibitors) and incubated on ice for 20 min. Lysates were passed through a 22-G syringe needle 15× and then centrifuged at 14,000 ×g for 2 min at 4°C. Supernatants were collected and re-centrifuged for 2 min to remove any remaining soluble material. Pellets were then combined and solubilized in solubilizing buffer (50mM Tris-HCl, pH 8.8; 5mM EDTA, 1% SDS).

Spectral-count proteomic analysis—ER-PM junction fractions were resuspended in Lameli buffer (BioRad) and run on Mini-PROTEAN 4%–20% TGX gels (BioRad) until the sample entered the gel. Bands were then excised. The proteins in the gel bands were reduced with DTT to break disulfide bonds, and the Cys residues were alkylated by iodoacetamide to allow the recovery of Cys-containing peptides. The gel bands were then washed, dried in a speed vacuum, and rehydrated with a buffer containing a protease to enable the protease to enter the gel. Typically, trypsin enzyme is used for digesting proteins, but additional enzymes may be used to achieve better coverage of protein sequence. In this experiment, each band was digested independently with trypsin and analyzed by mass spectrometry (MS). Raw data files for each sample were combined prior to database search. The peptide samples were loaded on a nanoscale capillary reverse-phase C18 column (2.7 μm C18, 100 mm) by an HPLC system (Waters ACQUITY UPLC or Thermo EASY-nLC 1000) and eluted by a gradient (~60 min). The eluted peptides were ionized and detected by an inline mass spectrometer (Thermo Fusion). MS data were collected first (in ~0.5 s), followed by sequential isolation for MS/MS analysis (each in ~0.1 s, totaling ~2 s) acquisition of the top-10 abundant ions and additional target Mz representing user-selected sites. This process (~2.5 s) was repeated over the entire elution chromatography gradient, acquiring more than 75,000 MS/MS spectra during a 180-min elution.

Database searches were performed using Sequest search engine in Thermo Proteome Discoverer 1.4 (v1.4.0.288) and PEAKS Studio 8.5 (Build 20180507) software packages. All matched MS/MS data were filtered by mass accuracy and matching scores to reduce the protein false-discovery rate to ~5%. Modification sites were determined by dynamically assigning related mass addition to all possible amino acid residues during the database search. Peptide assignments were further analyzed by Ascore, pRS score, and *de novo* sequencing programs and were subjected to manual examination. All proteins identified in a gel lane were combined. The total number of spectra, namely spectral counts, matching individual proteins may reflect their relative abundance in one sample, after the protein size is normalized. Moreover, the spectral count is useful for comparing the levels of the same protein across multiple samples (e.g., control and immunoprecipitated samples). Modified residues were further validated by an independent *de novo* sequencing of raw spectra and confirmed based on the unambiguous assignment of characteristic site-specific fragment ions. In addition, the ion intensities of modified peptides and corresponding

unmodified counterparts were compared to evaluate the stoichiometry of the modification events. Pathway analyses was performed using Ingenuity Pathway Analysis (IPA).

Golgi-Cox immunohistochemical staining—Golgi-Cox staining was performed using FD Rapid GolgiStain Kit (FD NeuroTechnologies). In short, 6-month-old mice were euthanized by CO_2 and brains were quickly isolated. The brains were rinsed with Milli-Q water to remove blood and immersed in impregnation solution (FD NeuroTechnologies) for 2 weeks at RT in the dark. The brains were transferred to development solution (FD NeuroTechnologies) for 72 h at RT in the dark. Brains were then flash-frozen in liquid nitrogen and cut into 100- to 200-μm sections on a cryostat. The brain sections were mounted on gelatin-coated slides and developed with staining solution (FD NeuroTechnologies). Sections were then dehydrated in 50%, 75%, and 95% ethanol for 4 min each. The sections were further dehydrated in 100% ethanol 4× for 4 min each. Sections were then cleared with xylene 3× for 4 min each and mounted in Cytoseal (Fischer) with a coverslip.

3D reconstruction of dendritic spines—For 3D reconstruction of Golgi-Cox–stained hippocampal pyramidal cells, Z-step brightfield images (60× oil immersion lens) were taken using the Lionheart FX automated microscope (Biotek), which enabled us to visualize dendritic spines. We performed linear deconvolution using ImageJ software and exported images to Imaris Imaging software for 3D reconstruction of the cells/tissue. Dendritic branches and spines were traced using the Filament Tracer software in a semiautomated fashion. Similar thresholds were used for spine-density seeding to enable the software to reconstruct the spines. Data readouts show the number of spines per 10-μm length of the dendritic branch.

GM1 isolation and quantification by HPTLC—To extract the lipids from the ER-PM junction fractions, we resuspended the ER-PM pellets in 3× volume of HPLC-grade water in an Eppendorf tube. An 8× volume of methanol was added to each sample (8:3 volume CH_3OH:dH_2O) and vortexed at RT. Chloroform equaling half the volume used for methanol was added to each sample (4:8:3 volume $CHCl_3$:CH_3OH:dH_2O) and vortexed at RT. The mixture was then centrifuged at 1200 ×*g* for 15 min at RT. The volume of supernatant was measured and transferred into a fresh Eppendorf tube. Water (0.173× the volume) was added to the supernatant, vortexed, and centrifuged at 1200 ×*g* for 15 min at RT. The upper polar phase was collected in a new tube and evaporated at 48°C overnight, until the lipid pellet remained. To analyze the GM1 content, we resuspended lipid pellets in 20–50 μL chloroform solution (4:8:3, $CHCl_3$:CH_3OH:dH_2O). A sample (5 μL) was loaded onto a 10 × 20 cm silicone-coated TLC plate (Millipore) using the Automatic TLC Sampler ATS 4 (Camag). GM1 (1 μg/μL) isolated from bovine brain (Sigma, Cat no. G7641) in the 4:8:3, $CHCl_3$:CH_3OH:dH_2O solution was plated as a standard. Plates were developed in an Automatic Developing Chamber ADC2 (Camag) using 60:35:8, $CHCl_3$:CH_3OH:0.25% KCl as development solution. Plates were then sprayed with resolving solution (2% resorcinol, 80% HCl, 5% 0.1M copper sulfate) and heated on a hot plate for 30 min at 95°C, until bands appeared. Plates were imaged on the TLC Visualizer 2 (Camag), and bands containing GM1 were quantified using the GM1 standard.

Immunoblotting and co-immunoprecipitation—For immunoblotting, samples were homogenized with RIPA buffer, and protein concentrations were determined using the Pierce BCA kit (Thermo Scientific). Proteins were separated by SDS–PAGE on precast Mini-PROTEAN 4%–20% TGX gels (BioRad), under reducing conditions. They were then transferred to a polyvinylidene difluoride (PVDF) membrane (Millipore). Membranes were incubated for 1 h in blocking buffer (5% dry milk in TBS-Tween) at RT and subsequently probed with the specific primary antibody diluted in 5% BSA/TBS-Tween overnight at 4 °C at the following concentrations: anti-BDNF, 1:1000 (Abcam); anti-pan calcineurin A, 1:1000 (Cell Signaling); anti-calnexin, 1:1000 (Novus Biologicals); anti-CaMKII, 1:500 (Santa Cruz); anti-ERK1/2, 1:1000 (Cell Signaling); anti-flotillin-1, 1:500 (BD Biosciences); anti-laminin A/C, 1:1000 (Cell Signaling); anti-LDH, 1:1000 (Chemicon); anti-N-cadherin, 1:1000 (BD Biosciences); anti-NMDAR-type 1 subunit, 1:1000 (Cell Signaling); anti-ORAI1, 1:500 (Abcam); anti-pERK1/2, 1:1000 (Cell Signaling); anti-PI4K, 1:1000 (Cell Signaling); anti-PIP5K1A, 1:1000 (Cell Signaling); anti-pNMDAR (Ser896), 1:1000 (Invitrogen); anti-STIM1, 1:1000 (Cell Signaling); anti-STIM2, 1:1000 (Cell Signaling); anti-TMEM24, 1:1000 (Fitzgerald); anti-TOMM20, 1:1000 (Santa Cruz); anti-TRKB, 1:1000 (Cell Signaling); anti-VAPA, 1:1000 (Bethyl); anti-VAPB, 1:1000 (Bethyl); and CTX-B HRP-conjugated, 1:5000 (Invitrogen). Blots were then washed 3× with TBS-Tween for 5 min and incubated with the appropriate secondary antibody for 1 h at RT. Blots were washed 3× with TBS-Tween for 5 min and developed using the Clarity Max Western ECL Substrate (BioRad). Protein band intensity was normalized to loading using stain-free quantification. Values in the graphs are expressed as the relative change to the average WT levels for each protein.

For co-immunoprecipitation, the GEMs isolated from ER-PM junctions were diluted in 500 μL RIPA buffer containing 2× protease inhibitors. Lysates were precleared with 30 μL Pansorbin cells (Millipore Sigma) for 1 h at 4°C. Lysates were washed with RIPA and incubated with anti-NMDAR-type 1 antibody (1:50), anti-pNMDAR (Ser 896) (1:50), or CTX-B biotin-conjugated (1:100). The samples were then incubated overnight at 4°C under agitation. 20 μL Protein A beads (Cell Signaling) or 5 μL Streptavidin Magnetic beads (Vector Lab) for CTX_B were incubated for 1 h at 4°C. Samples were centrifuged at 10,000 ×*g* for 30 s at 4°C and placed on a magnetic strip, and supernatant was removed. Pellets were washed 3× with RIPA buffer and resuspended in Laemmli sample buffer (BioRad) before immunoblotting on precast Mini-PROTEAN 4%–20% TGX gels. Proteins were then transferred onto PVDF membranes and probed with HRP–conjugated CTX-B to visualize GM1.

Immunofluorescent imaging—For brain tissue fluorescent imaging, mice were perfused with 20 mL of PBS followed by perfusion with 20 mL of 4% PFA in PBS. Brains were isolated and stored in 4% PFA for 24 h. Isolated brains were transferred to 50-mL Falcon tube containing 20mL of 15% sucrose solution in PBS for 24 h at 4°C, followed by a 30% sucrose/PBS solution for 24 hrs at 4°C, or until the brains sunk to the bottom of the tube. Brains were separated into hemispheres and embedded into Tissue-Tek O.C.T. compound (Sakura) and frozen in liquid nitrogen. O.C.T. blocks were sectioned into 8 μm brain slices and mounted to slides using a ThermoFischer HM525 NX cryostat at −23°C. Brain sections

were fixed onto slides with 1% PFA in PBS for 15 min at RT and washed 3× with PBS. Slides were transferred to 0.2% Triton X-100 and sections were permeabilized for 15 min at RT. Brain sections were blocked in blocking buffer containing 5% goat serum and 0.1% Triton X-100 in PBS for 1 h at RT. Brain sections were incubated in 1:1000 anti-PSD-95 antibody and 1:1000 anti-synaptophysin 1 antibody in blocking buffer overnight at 4°C. Slides were washed 3× in 0.1% Triton X-100/PBS for 5 min at RT. Brain sections were incubated in 1:400 goat anti-guinea pig Alexa Fluor 488-conjugated IgG secondary antibody (Invitrogen) and 1:400 goat anti-rabbit Alexa Fluor 568-conjugated IgG secondary antibody (Invitrogen) for 1 h at RT. Slides were washed 3× with PBS and mounted to coverslips using ProLong Gold antifade reagent with DAPI. Fluorescence slide scanning was performed using a Zeiss Axio Scan.Z1 with a Hamamatsu ORCA-Flash4.0 V3 camera using Zeiss ZEN 3.1 software. Images were created with a Zeiss Plan-Apochromat 20X/0.8 objective lens with illumination by Zeiss Colibri.2 LEDs (365nm, 470nm, 555nm) and corresponding filters (Zeiss Filter Set 49, 38 HE, and 43 HE, respectively). Fluorescence intensity was measured using ImageJ analysis software.

For cellular fluorescent imaging, primary Neurons were isolated from P5 WT mice and *β-Gal*$^{-/-}$ mice were cultured for 10 days and permeabilized and fixed using cold acetone for 5 min at −20°C. Cells were washed 3× with PBS and blocked in 0.25% Casine in PBS for 1 h at RT. Cells were incubated in 1:100 anti-NMDAR-type 1 subunit antibody and 1:1000 CTX-B Alexa Fluor 555-conjugated overnight at 4°C. Cells were washed 3× in PBS and incubated with donkey anti-rabbit Alexa Fluor 488-conjugated IgG secondary antibody (Invitrogen) for 1 h at RT. Cells were washed and mounted on a coverslip using ProLong Gold Antifade Mountant with DNA Stain DAPI (ThermoFisher). The amount of colocalized area was calculated using Imaris.

Ca^{2+} imaging *in vitro*—HeLa cells and primary neurons were put into culture in a 2-well glass bottom slide (LabTek) using the methods described above and 1 mL of the appropriate media described. Media was aspirated, and cells were transduced with 10 μL Lenti-Gcamp6s construct in 500 μL media for 4 h at 37°C in 5% CO_2. Media was removed and cells were washed 2× with PBS for 5 min. Media (1 mL) was added to the cells, and slides were incubated at 37°C in 5% CO_2 overnight. To load HeLa cells with GM1, 1 μg/μL GM1 was added overnight in 0.5% serum media. Slides were then imaged on the Marianas 2Axio Observer microscope at 37°C in 5% CO_2 in the green fluorescence channel (488 nm). z stack imaging was performed on the entire cell body, and maximum-intensity projections were performed on 2D flattened images.

QUANTIFICATION AND STATISTICAL ANALYSES

Statistical analyses were performed using GraphPad Prism. Quantitative data are presented as median ± quartiles, or as mean ± 95% confidence interval (MAPPER experiment). For comparisons between 2 groups, Student's *t*-tests (paired or unpaired, 2-tailed) were performed. For small sample sizes ($n < 6$), a Welch's correction was applied to the Student's *t*-test. For comparisons of 3 or more groups, one-way or two-way ANOVAs were performed. *p*P-values <0.5 were considered statistically significant. The number of samples is indicated

in the figure legends. For IPA pathway analyses, top canonical pathways were reported with a Fischer's Exact test *pp*-value above a threshold of 0.05.

Supplementary Material

Refer to Web version on PubMed Central for supplementary material.

ACKNOWLEDGMENTS

We thank Dr. Xiaohui Qiu for help with the production of lentiviruses. We gratefully acknowledge Dr. Angela McArthur (St. Jude Department of Scientific Editing) for editing the manuscript. We would also like to thank Dr. George Campbell and Dr. Aaron Pitre with the St. Jude Cell and Tissue Imaging Center for their assistance in planning microscopy experiments. A.d'A. holds the Jewelers for Children Endowed Chair in Genetics and Gene Therapy. This work was supported in part by NIH grants, DK052025 and CA021764 and grants from the Assisi Foundation of Memphis, the National Tay-Sachs and Allied Diseases, Inc. (NTSAD), and the American Lebanese Syrian Associated Charities (ALSAC). The content is solely the responsibility of the authors and does not necessarily represent the official views of the National Institutes of Health.

REFERENCES

1. Bravo-Sagua R, Torrealba N, Paredes F, Morales PE, Pennanen C, López-Crisosto C, Troncoso R, Criollo A, Chiong M, Hill JA, et al. (2014). Organelle communication: Signaling crossroads between homeostasis and disease. Int. J. Biochem. Cell Biol. 50, 55–59. 10.1016/j.biocel.2014.01.019. [PubMed: 24534274]
2. Jing J, Liu G, Huang Y, and Zhou Y (2020). A molecular toolbox for interrogation of membrane contact sites. J. Physiol. 598, 1725–1739. 10.1113/jp277761. [PubMed: 31119749]
3. Scorrano L, De Matteis MA, Emr S, Giordano F, Hajnóczky G, Kornmann B, Lackner LL, Levine TP, Pellegrini L, Reinisch K, et al. (2019). Coming together to define membrane contact sites. Nat. Commun. 10, 1287. 10.1038/s41467-019-09253-3. [PubMed: 30894536]
4. Prinz WA, Toulmay A, and Balla T (2020). The functional universe of membrane contact sites. Nat. Rev. Mol. Cell Biol. 21, 7–24. 10.1038/s41580-019-0180-9. [PubMed: 31732717]
5. Vance JE (2020). Inter-organelle membrane contact sites: implications for lipid metabolism. Biol. Direct 15, 24. 10.1186/s13062-020-00279-y. [PubMed: 33176847]
6. Burgoyne T, Patel S, and Eden ER (2015). Calcium signaling at ER membrane contact sites. Biochim. Biophys. Acta 1853, 2012–2017. 10.1016/j.bbamcr.2015.01.022. [PubMed: 25662816]
7. Aoyama-Ishiwatari S, and Hirabayashi Y (2021). Endoplasmic Reticulum–Mitochondria Contact Sites—Emerging Intracellular Signaling Hubs. Front. Cell Dev. Biol. 9, 653828. 10.3389/fcell.2021.653828. [PubMed: 34095118]
8. Weesner JA, Annunziata I, van de Vlekkert D, and d'Azzo A (2023). Glycosphingolipids within membrane contact sites influence their function as signaling hubs in neurodegenerative diseases. FEBS Open Bio. 13, 1587–1600. 10.1002/2211-5463.13605.
9. Li C, Qian T, He R, Wan C, Liu Y, and Yu H (2021). Endoplasmic Reticulum-Plasma Membrane Contact Sites: Regulators, Mechanisms, and Physiological Functions. Front. Cell Dev. Biol. 9, 627700. 10.3389/fcell.2021.627700. [PubMed: 33614657]
10. Porter KR, and Palade GE (1957). Studies on the endoplasmic reticulum: III. Its form and distribution in striated muscle cells. J. Biophys. Biochem. Cytol. 3, 269–300. 10.1083/jcb.3.2.269. [PubMed: 13438910]
11. Rosenbluth J (1962). Subsurface cisterns and their relationship to the neuronal plasma membrane. J. Cell Biol. 13, 405–421. 10.1083/jcb.13.3.405. [PubMed: 14493991]
12. Wu Y, Whiteus C, Xu CS, Hayworth KJ, Weinberg RJ, Hess HF, and De Camilli P (2017). Contacts between the endoplasmic reticulum and other membranes in neurons. Proc. Natl. Acad. Sci. USA 114, E4859–E4867. 10.1073/pnas.1701078114. [PubMed: 28559323]
13. Takano T, Funahashi Y, and Kaibuchi K (2019). Neuronal Polarity: Positive and Negative Feedback Signals. Front. Cell Dev. Biol. 7, 69. 10.3389/fcell.2019.00069. [PubMed: 31069225]

14. Romaus-Sanjurjo D, Custodia A, Aramburu-Núñez M, Posado-Fernández A, Vázquez-Vázquez L, Camino-Castiñeiras J, Leira Y, Pías-Peleteiro JM, Aldrey JM, Ouro A, and Sobrino T (2021). Symmetric and Asymmetric Synapses Driving Neurodegenerative Disorders. Symmetry 13, 2333. 10.3390/sym13122333.
15. Pchitskaya E, and Bezprozvanny I (2020). Dendritic Spines Shape Analysis—Classification or Clusterization? Perspective. Front. Synaptic Neurosci. 12, 31. 10.3389/fnsyn.2020.00031. [PubMed: 33117142]
16. Lüscher C, and Malenka RC (2012). NMDA receptor-dependent long-term potentiation and long-term depression (LTP/LTD). Cold Spring Harb. Perspect. Biol. 4, a005710. 10.1101/cshperspect.a005710. [PubMed: 22510460]
17. Park M (2018). AMPA Receptor Trafficking for Postsynaptic Potentiation. Front. Cell. Neurosci. 12, 361. 10.3389/fncel.2018.00361. [PubMed: 30364291]
18. Chen B-S, and Roche KW (2007). Regulation of NMDA receptors by phosphorylation. Neuropharmacology 53, 362–368. 10.1016/j.neuropharm.2007.05.018. [PubMed: 17644144]
19. Wang JQ, Arora A, Yang L, Parelkar NK, Zhang G, Liu X, Choe ES, and Mao L (2005). Phosphorylation of AMPA receptors: mechanisms and synaptic plasticity. Mol. Neurobiol. 32, 237–249. 10.1385/mn:32:3:237. [PubMed: 16385140]
20. Zaman MF, Nenadic A, Radojičić A, Rosado A, and Beh CT (2020). Sticking With It: ER-PM Membrane Contact Sites as a Coordinating Nexus for Regulating Lipids and Proteins at the Cell Cortex. Front. Cell Dev. Biol. 8, 675. 10.3389/fcell.2020.00675. [PubMed: 32793605]
21. Chen Y-J, Quintanilla CG, and Liou J (2019). Recent insights into mammalian ER-PM junctions. Curr. Opin. Cell Biol. 57, 99–105. 10.1016/j.ceb.2018.12.011. [PubMed: 30739879]
22. Ong HL, and Ambudkar IS (2020). The Endoplasmic Reticulum-Plasma Membrane Junction: A Hub for Agonist Regulation of Ca(2+) Entry. Cold Spring Harb. Perspect. Biol. 12, a035253. 10.1101/cshperspect.a035253. [PubMed: 31501196]
23. Hogan PG, and Rao A (2015). Store-operated calcium entry: Mechanisms and modulation. Biochem. Biophys. Res. Commun. 460, 40–49. 10.1016/j.bbrc.2015.02.110. [PubMed: 25998732]
24. Trebak M, and Putney JW Jr. (2017). ORAI Calcium Channels. Physiology 32, 332–342. 10.1152/physiol.00011.2017. [PubMed: 28615316]
25. Dickson EJ, Jensen JB, Vivas O, Kruse M, Traynor-Kaplan AE, and Hille B (2016). Dynamic formation of ER-PM junctions presents a lipid phosphatase to regulate phosphoinositides. J. Cell Biol. 213, 33–48. 10.1083/jcb.201508106. [PubMed: 27044890]
26. Bian X, Saheki Y, and De Camilli P (2018). Ca2+ releases E-Syt1 autoinhibition to couple ER-plasma membrane tethering with lipid transport. EMBO J. 37, 219–234. 10.15252/embj.201797359. [PubMed: 29222176]
27. Lees JA, Messa M, Sun EW, Wheeler H, Torta F, Wenk MR, De Camilli P, and Reinisch KM (2017). Lipid transport by TMEM24 at ER-plasma membrane contacts regulates pulsatile insulin secretion. Science 355, eaah6171. 10.1126/science.aah6171. [PubMed: 28209843]
28. Sun EW, Guillén-Samander A, Bian X, Wu Y, Cai Y, Messa M, and De Camilli P (2019). Lipid transporter TMEM24/C2CD2L is a Ca(2+)-regulated component of ER-plasma membrane contacts in mammalian neurons. Proc. Natl. Acad. Sci. USA 116, 5775–5784. 10.1073/pnas.1820156116. [PubMed: 30819882]
29. Quintanilla CG, Lee WR, and Liou J (2022). Nir1 constitutively localizes at ER-PM junctions and promotes Nir2 recruitment for PIP(2) homeostasis. Mol. Biol. Cell 33, br2. 10.1091/mbc.E21-07-0356. [PubMed: 35020418]
30. Tariq K, and Luikart BW (2021). Striking a balance: PIP(2) and PIP(3) signaling in neuronal health and disease. Explor. Neuroprotective Ther. 1, 86–100. 10.37349/ent.2021.00008. [PubMed: 35098253]
31. Guillén-Samander A, Wu Y, Pineda SS, García FJ, Eisen JN, Leonzino M, Ugur B, Kellis M, Heiman M, and De Camilli P (2022). A partnership between the lipid scramblase XK and the lipid transfer protein VPS13A at the plasma membrane. Proc. Natl. Acad. Sci. USA 119, e2205425119. 10.1073/pnas.2205425119. [PubMed: 35994651]

32. Schnaar RL, Gerardy-Schahn R, and Hildebrandt H (2014). Sialic acids in the brain: gangliosides and polysialic acid in nervous system development, stability, disease, and regeneration. Physiol. Rev. 94, 461–518. 10.1152/physrev.00033.2013. [PubMed: 24692354]
33. Sipione S, Monyror J, Galleguillos D, Steinberg N, and Kadam V (2020). Gangliosides in the Brain: Physiology, Pathophysiology and Therapeutic Applications. Front. Neurosci. 14, 572965. 10.3389/fnins.2020.572965. [PubMed: 33117120]
34. Ledeen RW, and Wu G (2015). The multi-tasked life of GM1 ganglioside, a true factotum of nature. Trends Biochem. Sci. 40, 407–418. 10.1016/j.tibs.2015.04.005. [PubMed: 26024958]
35. Chiricozzi E, Lunghi G, Di Biase E, Fazzari M, Sonnino S, and Mauri L (2020). GM1 Ganglioside Is A Key Factor in Maintaining the Mammalian Neuronal Functions Avoiding Neurodegeneration. Int. J. Mol. Sci. 21, 868. 10.3390/ijms21030868. [PubMed: 32013258]
36. Sano R, Annunziata I, Patterson A, Moshiach S, Gomero E, Opferman J, Forte M, and d'Azzo A (2009). GM1-Ganglioside Accumulation at the Mitochondria-Associated ER Membranes Links ER Stress to Ca2+--Dependent Mitochondrial Apoptosis. Mol. Cell 36, 500–511. 10.1016/j.molcel.2009.10.021. [PubMed: 19917257]
37. Moreno-Altamirano MMB, Aguilar-Carmona I, and Sánchez-García FJ (2007). Expression of GM1, a marker of lipid rafts, defines two subsets of human monocytes with differential endocytic capacity and lipopolysaccharide responsiveness. Immunology 120, 536–543. 10.1111/j.1365-2567.2006.02531.x. [PubMed: 17250589]
38. Nichols BJ (2003). GM1-Containing Lipid Rafts Are Depleted within Clathrin-Coated Pits. Curr. Biol. 13, 686–690. 10.1016/S0960-9822(03)00209-4. [PubMed: 12699627]
39. Wu G, Lu ZH, Nakamura K, Spray DC, and Ledeen RW (1996). Trophic effect of cholera toxin B subunit in cultured cerebellar granule neurons: modulation of intracellular calcium by GM1 ganglioside. J. Neurosci. Res. 44, 243–254. 10.1002/(sici)1097-4547(19960501)44:3<243::Aid-jnr5>3.0.Co;2-g. [PubMed: 8723763]
40. Rawal P, and Zhao L (2021). Sialometabolism in brain health and Alzheimer's disease. Front. Neurosci. 15, 648617. 10.3389/fnins.2021.648617. [PubMed: 33867926]
41. Duchemin AM, Ren Q, Mo L, Neff NH, and Hadjiconstantinou M (2002). GM1 ganglioside induces phosphorylation and activation of Trk and Erk in brain. J. Neurochem. 81, 696–707. 10.1046/j.1471-4159.2002.00831.x. [PubMed: 12065629]
42. Lim ST, Esfahani K, Avdoshina V, and Mocchetti I (2011). Exogenous gangliosides increase the release of brain-derived neurotrophic factor. Neuropharmacology 60, 1160–1167. 10.1016/j.neuropharm.2010.10.012. [PubMed: 20971126]
43. Nicoli E-R, Annunziata I, d'Azzo A, Platt FM, Tifft CJ, and Stepien KM (2021). GM1 Gangliosidosis—A Mini-Review. Front. Genet. 12, 734878. 10.3389/fgene.2021.734878. [PubMed: 34539759]
44. Rha AK, Maguire AS, and Martin DR (2021). GM1 Gangliosidosis: Mechanisms and Management. Appl. Clin. Genet. 14, 209–233. 10.2147/tacg.S206076. [PubMed: 33859490]
45. Hahn CN, del Pilar Martin M, Schröder M, Vanier MT, Suzuki K, Hara Y, Suzuki K, and d'Azzo A (1997). Generalized CNS Disease and Massive GM1-Ganglioside Accumulation in Mice Defective in Lysosomal Acid β-galactosidase. Hum. Mol. Genet. 6, 205–211. 10.1093/hmg/6.2.205. [PubMed: 9063740]
46. Jeyakumar M, Thomas R, Elliot-Smith E, Smith DA, van der Spoel AC, d'Azzo A, Perry VH, Butters TD, Dwek RA, and Platt FM (2003). Central nervous system inflammation is a hallmark of pathogenesis in mouse models of GM1 and GM2 gangliosidosis. Brain 126, 974–987. 10.1093/brain/awg089. [PubMed: 12615653]
47. Tessitore A, del P Martin M, Sano R, Ma Y, Mann L, Ingrassia A, Laywell ED, Steindler DA, Hendershot LM, d'Azzo A, and d'Azzo A (2004). GM1-Ganglioside-Mediated Activation of the Unfolded Protein Response Causes Neuronal Death in a Neurodegenerative Gangliosidosis. Mol. Cell 15, 753–766. 10.1016/j.molcel.2004.08.029. [PubMed: 15350219]
48. Baker HJ, Reynolds GD, Walkley SU, Cox NR, and Baker GH (1979). The Gangliosidoses: Comparative Features and Research Applications. Vet. Pathol. 16, 635–649. 10.1177/030098587901600602. [PubMed: 116415]

49. Chang C-L, Hsieh T-S, Yang TT, Rothberg KG, Azizoglu DB, Volk E, Liao J-C, and Liou J (2013). Feedback Regulation of Receptor-Induced Ca2+ Signaling Mediated by E-Syt1 and Nir2 at Endoplasmic Reticulum-Plasma Membrane Junctions. Cell Rep. 5, 813–825. 10.1016/j.celrep.2013.09.038. [PubMed: 24183667]
50. Krapivinsky G, Krapivinsky L, Manasian Y, Ivanov A, Tyzio R, Pellegrino C, Ben-Ari Y, Clapham DE, and Medina I (2003). The NMDA receptor is coupled to the ERK pathway by a direct interaction between NR2B and RasGRF1. Neuron 40, 775–784. 10.1016/s0896-6273(03)00645-7. [PubMed: 14622581]
51. Scott DB, Blanpied TA, and Ehlers MD (2003). Coordinated PKA and PKC phosphorylation suppresses RXR-mediated ER retention and regulates the surface delivery of NMDA receptors. Neuropharmacology 45, 755–767. 10.1016/S0028-3908(03)00250-8. [PubMed: 14529714]
52. Sakai N, Yamada M, Numakawa T, Ogura A, and Hatanaka H (1997). BDNF potentiates spontaneous Ca2+ oscillations in cultured hippocampal neurons. Brain Res. 778, 318–328. 10.1016/s0006-8993(97)01052-4. [PubMed: 9459549]
53. Levine ES, Crozier RA, Black IB, and Plummer MR (1998). Brain-derived neurotrophic factor modulates hippocampal synaptic transmission by increasing N-methyl-D-aspartic acid receptor activity. Proc. Natl. Acad. Sci. USA 95, 10235–10239. 10.1073/pnas.95.17.10235. [PubMed: 9707630]
54. Balla A, Tuymetova G, Barshishat M, Geiszt M, and Balla T (2002). Characterization of type II phosphatidylinositol 4-kinase isoforms reveals association of the enzymes with endosomal vesicular compartments. J. Biol. Chem. 277, 20041–20050. 10.1074/jbc.M111807200. [PubMed: 11923287]
55. Balla A, Vereb G, Gülkan H, Gehrmann T, Gergely P, Heilmeyer LM Jr., and Antal M (2000). Immunohistochemical localisation of two phosphatidylinositol 4-kinase isoforms, PI4K230 and PI4K92, in the central nervous system of rats. Exp. Brain Res. 134, 279–288. 10.1007/s002210000469. [PubMed: 11045352]
56. Alonso M, Medina JH, and Pozzo-Miller L (2004). ERK1/2 activation is necessary for BDNF to increase dendritic spine density in hippocampal CA1 pyramidal neurons. Learn. Mem. 11, 172–178. 10.1101/lm.67804. [PubMed: 15054132]
57. Ying SW, Futter M, Rosenblum K, Webber MJ, Hunt SP, Bliss TVP, and Bramham CR (2002). Brain-derived neurotrophic factor induces long-term potentiation in intact adult hippocampus: requirement for ERK activation coupled to CREB and upregulation of Arc synthesis. J. Neurosci. 22, 1532–1540. 10.1523/jneurosci.22-05-01532.2002. [PubMed: 11880483]
58. Faddis BT, Hasbani MJ, and Goldberg MP (1997). Calpain Activation Contributes to Dendritic Remodeling after Brief Excitotoxic Injury *In Vitro*. J. Neurosci. 17, 951–959. 10.1523/jneurosci.17-03-00951.1997. [PubMed: 8994050]
59. Greenwood SM, Mizielinska SM, Frenguelli BG, Harvey J, and Connolly CN (2007). Mitochondrial Dysfunction and Dendritic Beading during Neuronal Toxicity. J. Biol. Chem. 282, 26235–26244. 10.1074/jbc.M704488200. [PubMed: 17616519]
60. Ferreras S, Fernández G, Danelon V, Pisano MV, Masseroni L, Chapleau CA, Krapacher FA, Mlewski EC, Mascó DH, Arias C, et al. (2017). Cdk5 Is Essential for Amphetamine to Increase Dendritic Spine Density in Hippocampal Pyramidal Neurons. Front. Cell. Neurosci. 11. 10.3389/fncel.2017.00372.
61. Chen Y, Rex CS, Rice CJ, Dubé CM, Gall CM, Lynch G, and Baram TZ (2010). Correlated memory defects and hippocampal dendritic spine loss after acute stress involve corticotropin-releasing hormone signaling. Proc. Natl. Acad. Sci. USA 107, 13123–13128. 10.1073/pnas.1003825107. [PubMed: 20615973]
62. Yang Y, Wang X. b., Frerking M, and Zhou Q (2008). Spine expansion and stabilization associated with long-term potentiation. J. Neurosci. 28, 5740–5751. 10.1523/JNEUROSCI.3998-07.2008. [PubMed: 18509035]
63. Mandal M, and Yan Z (2009). Phosphatidylinositol (4,5)-Bisphosphate Regulation of N-Methyl-d-aspartate Receptor Channels in Cortical Neurons. Mol. Pharmacol. 76, 1349–1359. 10.1124/mol.109.058701. [PubMed: 19770351]
64. Dotti CG, Esteban JA, and Ledesma MD (2014). Lipid dynamics at dendritic spines. Front. Neuroanat. 8, 76. 10.3389/fnana.2014.00076. [PubMed: 25152717]

65. Ultanir SK, Kim JE, Hall BJ, Deerinck T, Ellisman M, and Ghosh A (2007). Regulation of spine morphology and spine density by NMDA receptor signaling in vivo. Proc. Natl. Acad. Sci. USA 104, 19553–19558. 10.1073/pnas.0704031104. [PubMed: 18048342]

66. Mukherjee A, and Soto C (2011). Role of calcineurin in neurodegeneration produced by misfolded proteins and endoplasmic reticulum stress. Curr. Opin. Cell Biol. 23, 223–230. 10.1016/j.ceb.2010.12.006. [PubMed: 21295458]

67. Spires-Jones TL, Kay K, Matsouka R, Rozkalne A, Betensky RA, and Hyman BT (2011). Calcineurin inhibition with systemic FK506 treatment increases dendritic branching and dendritic spine density in healthy adult mouse brain. Neurosci. Lett. 487, 260–263. 10.1016/j.neulet.2010.10.033. [PubMed: 20970476]

68. Wu H-Y, Hudry E, Hashimoto T, Kuchibhotla K, Rozkalne A, Fan Z, Spires-Jones T, Xie H, Arbel-Ornath M, and Grosskreutz CL (2010). Amyloid β induces the morphological neurodegenerative triad of spine loss, dendritic simplification, and neuritic dystrophies through calcineurin activation. J. Neurosci. 30, 2636–2649. 10.1523/JNEUROSCI.4456-09.2010. [PubMed: 20164348]

69. Dougherty MK, Ritt DA, Zhou M, Specht SI, Monson DM, Veenstra TD, and Morrison DK (2009). KSR2 Is a Calcineurin Substrate that Promotes ERK Cascade Activation in Response to Calcium Signals. Mol. Cell 34, 652–662. 10.1016/j.molcel.2009.06.001. [PubMed: 19560418]

70. Martínez-Cerdeño V (2017). Dendrite and spine modifications in autism and related neurodevelopmental disorders in patients and animal models. Dev. Neurobiol. 77, 393–404. 10.1002/dneu.22417. [PubMed: 27390186]

71. Telias M (2019). Molecular Mechanisms of Synaptic Dysregulation in Fragile X Syndrome and Autism Spectrum Disorders. Front. Mol. Neurosci. 12. 10.3389/fnmol.2019.00051.

72. Penzes P, Cahill ME, Jones KA, VanLeeuwen JE, and Woolfrey KM (2011). Dendritic spine pathology in neuropsychiatric disorders. Nat. Neurosci. 14, 285–293. 10.1038/nn.2741. [PubMed: 21346746]

73. Chen TW, Wardill TJ, Sun Y, Pulver SR, Renninger SL, Baohan A, Schreiter ER, Kerr RA, Orger MB, Jayaraman V, et al. (2013). Ultrasensitive fluorescent proteins for imaging neuronal activity. Nature 499, 295–300. 10.1038/nature12354. [PubMed: 23868258]

74. Schneider CA, Rasband WS, and Eliceiri KW (2012). NIH Image to ImageJ: 25 years of image analysis. Nat. Methods 9, 671–675. 10.1038/nmeth.2089. [PubMed: 22930834]

75. Kremer JR, Mastronarde DN, and McIntosh JR (1996). Computer visualization of three-dimensional image data using IMOD. J. Struct. Biol. 116, 71–76. 10.1006/jsbi.1996.0013. [PubMed: 8742726]

76. Mastronarde DN (2005). Automated electron microscope tomography using robust prediction of specimen movements. J. Struct. Biol. 152, 36–51. 10.1016/j.jsb.2005.07.007. [PubMed: 16182563]

77. Hanawa H, Kelly PF, Nathwani AC, Persons DA, Vandergriff JA, Hargrove P, Vanin EF, and Nienhuis AW (2002). Comparison of Various Envelope Proteins for Their Ability to Pseudotype Lentiviral Vectors and Transduce Primitive Hematopoietic Cells from Human Blood. Mol. Ther. 5, 242–251. 10.1006/mthe.2002.0549. [PubMed: 11863413]

Highlights

- Neuronal accumulation of GM1 due to β-GAL deficiency increases ER-PM junction formation
- GM1 binds pNMDAR at the ER-PM junctions, altering intracellular Ca^{2+} concentration
- pNMDAR-mediated Ca^{2+} signaling and increased BDNF levels activate the ERK pathway
- Altered levels of GM1 increase synaptic spine formation without increasing connectivity

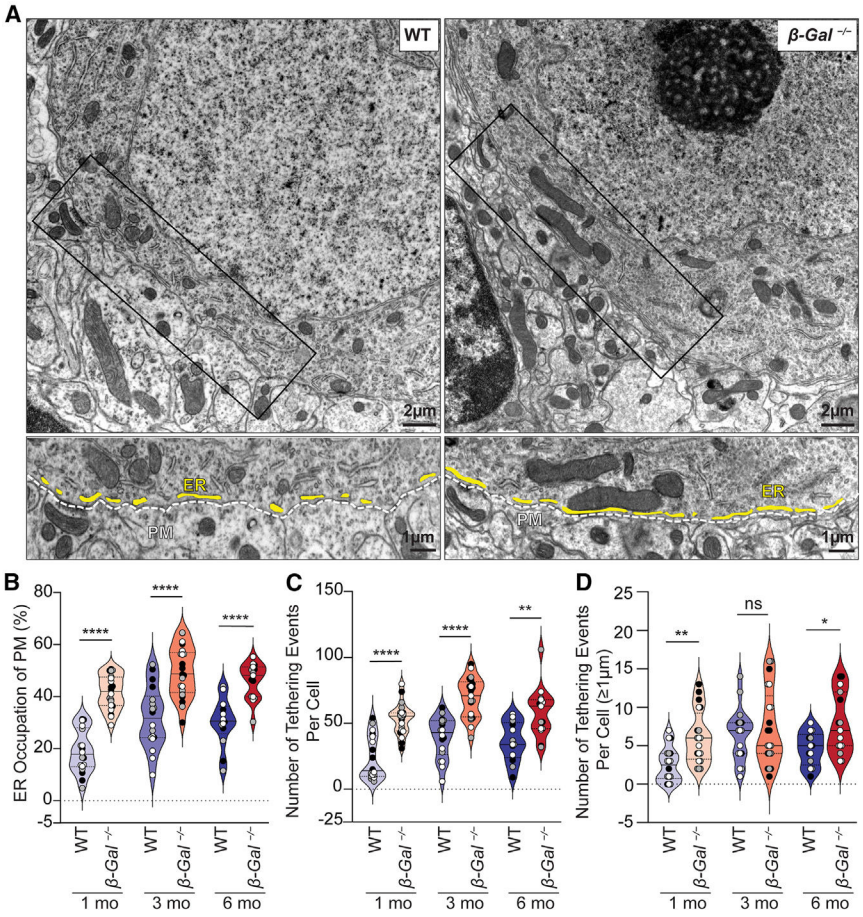

Figure 1. Increased formation of ER-PM junctions in *β-Gal*$^{-/-}$ Purkinje cells

(A) TEM images of Purkinje cells in 6-month-old WT and *β-Gal*$^{-/-}$ mice. Scale bar: 2 μm. Bottom images show 1.4× zoom of black boxes with highlighted PM (white line) and ER fragments (yellow lines). Scale bar: 1 μm.

(B) Quantification of the average length of ER occupation to the PM (percentage) in Purkinje cells from 1-, 3-, and 6-month-old WT and *β-Gal*$^{-/-}$ mice, expressed as percentage of the total cell perimeter. $n = 3$ mice; 5–9 Purkinje cells per mouse, each mouse is represented by a different colored filled datapoint (black, gray, white). Values are expressed as median ± quartiles. Statistical analysis was performed using the one-way ANOVA; ****$p < 0.0001$.

(C) Quantification of the total number of tethering events per cell in Purkinje cells from 1-, 3-, and 6-month-old WT and *β-Gal*$^{-/-}$ mice. $n = 3$ mice; 5–9 Purkinje cells per mouse, each mouse is represented by a different colored filled datapoint (black, gray, white). Values are expressed as median ± quartiles. Statistical analysis was performed using the one-way ANOVA; **$p < 0.01$, ****$p < 0.0001$.

(D) Quantification of the total number of tethering events greater than or equal to 1 μm in length per Purkinje cell from 1-, 3-, and 6-month-old WT and *β-Gal*$^{-/-}$ mice. $n = 3$ mice; 5–9 Purkinje cells per mouse, each mouse is represented by a different colored filled datapoint (black, gray, white). Values are expressed as median ± quartiles. Statistical analysis was performed using the one-way ANOVA; ns, not significant; *$p < 0.05$, **$p < 0.01$.

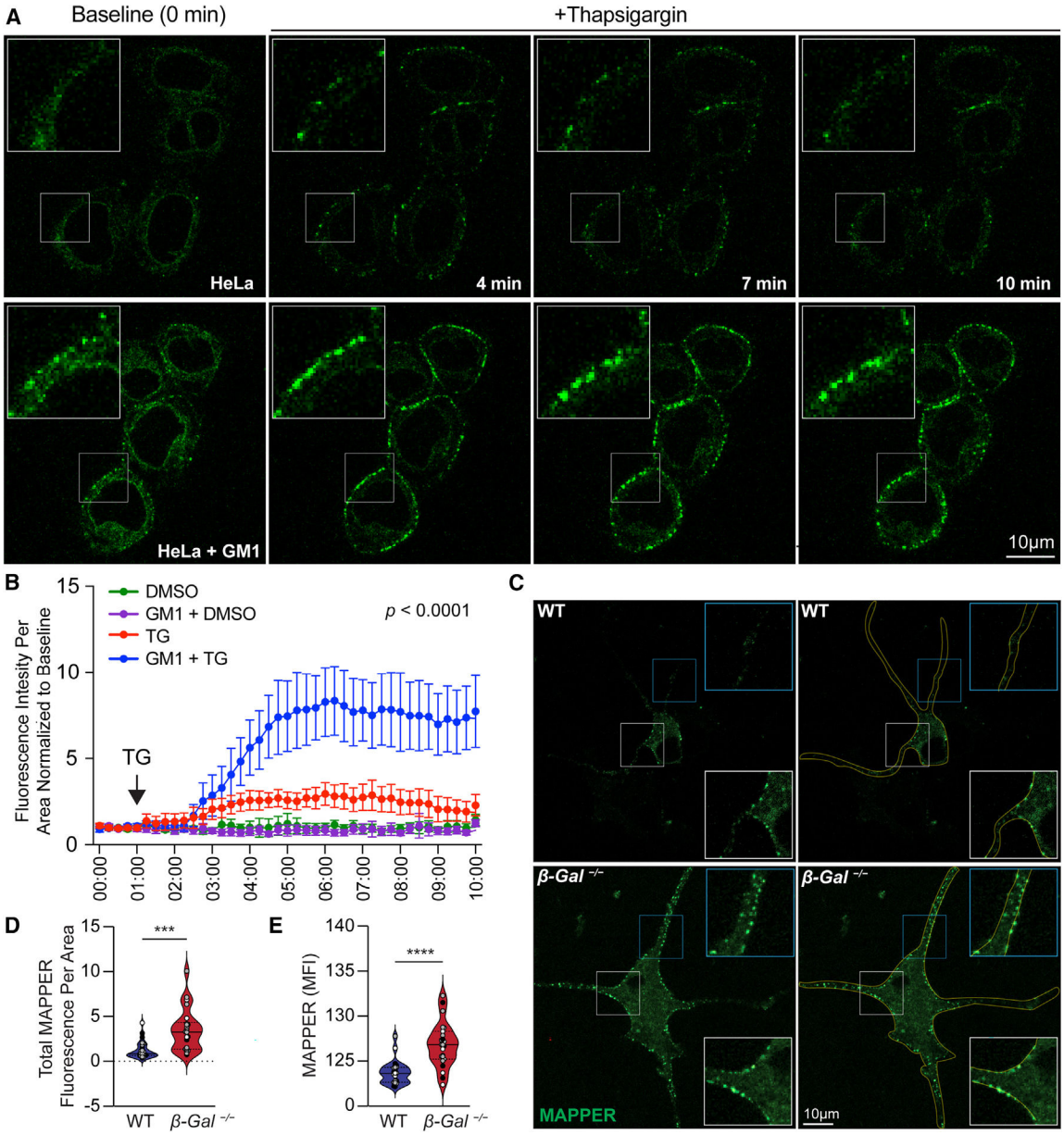

Figure 2. ER-PM junctions form in GM1-loaded HeLa cells and primary neurons

(A) Time-course confocal immunofluorescence of MAPPER-transduced HeLa cells (green). GM1 was exogenously added to HeLa cells. Images were captured at baseline (0 min) and at 4, 7, and 10 min post treatment with thapsigargin (TG). Scale bar: 10 μm. Inset images show 5× zoom of white boxes.

(B) Quantification of fluorescence intensity per area over time, normalized to baseline (0–10 min). Experiments were performed on HeLa cells in triplicate, and six or seven fields of view were analyzed; DMSO, $n = 19$; GM1 + DMSO, $n = 20$; TG, $n = 19$; and GM1 + TG, $n = 17$. Values are expressed as mean ± 95% confidence interval. Statistical analysis was performed using the two-Way ANOVA tests; $p < 0.0001$.

(C) Representative fluorescent images of MAPPER-transduced primary neurons isolated from P5 WT and *β-Gal*$^{-/-}$ pups. Images shown on the right panels are duplicate of those

on the left panels but have the contour of the neuronal cell body outlined in yellow. Green puncta along the cell surface (yellow outline) indicate ER-PM junctions. Scale bar: 10 μm. Inset images show 2× zoom of white (soma) and blue (dendrite) boxes.

(D) Quantification of total MAPPER fluorescence area per cell in primary neurons isolated from P5 WT and β-$Gal^{-/-}$ pups. $n = 3$ mice; 5–10 neurons per brain, each mouse is represented by a different colored filled datapoint (black, gray, white). Values are expressed as median ± quartiles. Statistical analysis was performed using the Student's t test; ***$p < 0.001$.

(E) Quantification of the mean fluorescence intensity (MFI) of $MAPPER^{+}$ puncta in primary neurons isolated from P5 WT and β-$Gal^{-/-}$ pups. $n = 3$ mice; 5–10 neurons per brain, each mouse is represented by a different colored filled datapoint (black, gray, white). Values are expressed as median ± quartiles. Statistical analysis was performed using the Student's t test; ****$p < 0.0001$.

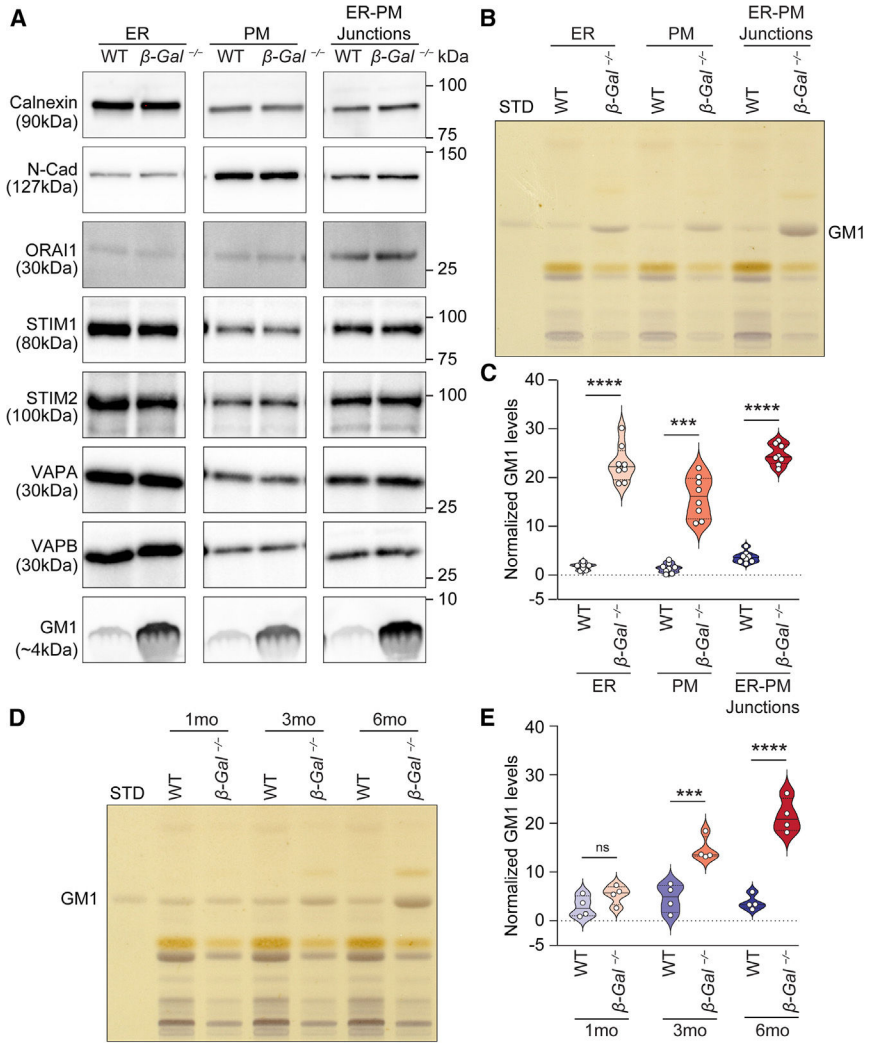

Figure 3. GM1 accumulates in *β-Gal*$^{-/-}$ ER-PM junctions

(A) Immunoblot analysis of cell fractions from 6-month-old WT and *β-Gal*$^{-/-}$ mice. Markers for the ER (Calnexin), PM (N-cadherin), and ER-PM junctions (ORAI1, STIM1, STIM2, VAPA, and VAPB) were enriched in their respective fractions. Immunoblots using HRP-conjugated cholera toxin B subunit (CTX-B) show high GM1 levels in *β-Gal*$^{-/-}$ fractions.

(B) Representative HPTLC plate showing GM1 levels in the ER, PM, and ER-PM junctions isolated from 6-month-old WT and *β-Gal*$^{-/-}$ mice. STD, standard. Note: to detect GM1 in WT samples, the sample volume loaded was 3× that of the *β-Gal*$^{-/-}$ samples.

(C) Quantification of GM1 levels from HPTLC plates performed in (B). $n = 8$. Values are expressed as median ± quartiles. Statistical analysis was performed using the Student's t test; ***$p < 0.001$, ****$p < 0.0001$.

(D) Representative HPTLC plate showing GM1 levels in ER-PM junctions isolated from 1-, 3-, and 6-month-old WT and *β-Gal*$^{-/-}$ mice. To detect GM1 in WT samples, the sample volume loaded was 3× that of the *β-Gal*$^{-/-}$ samples.

(E) Quantification of GM1 levels from HPTLC plates performed in (D). $n = 4$. Values are expressed as median ± quartiles. Statistical analysis was performed using the Student's t test with Welch's correction; ns, not significant; ***$p < 0.001$, ****$p < 0.0001$.

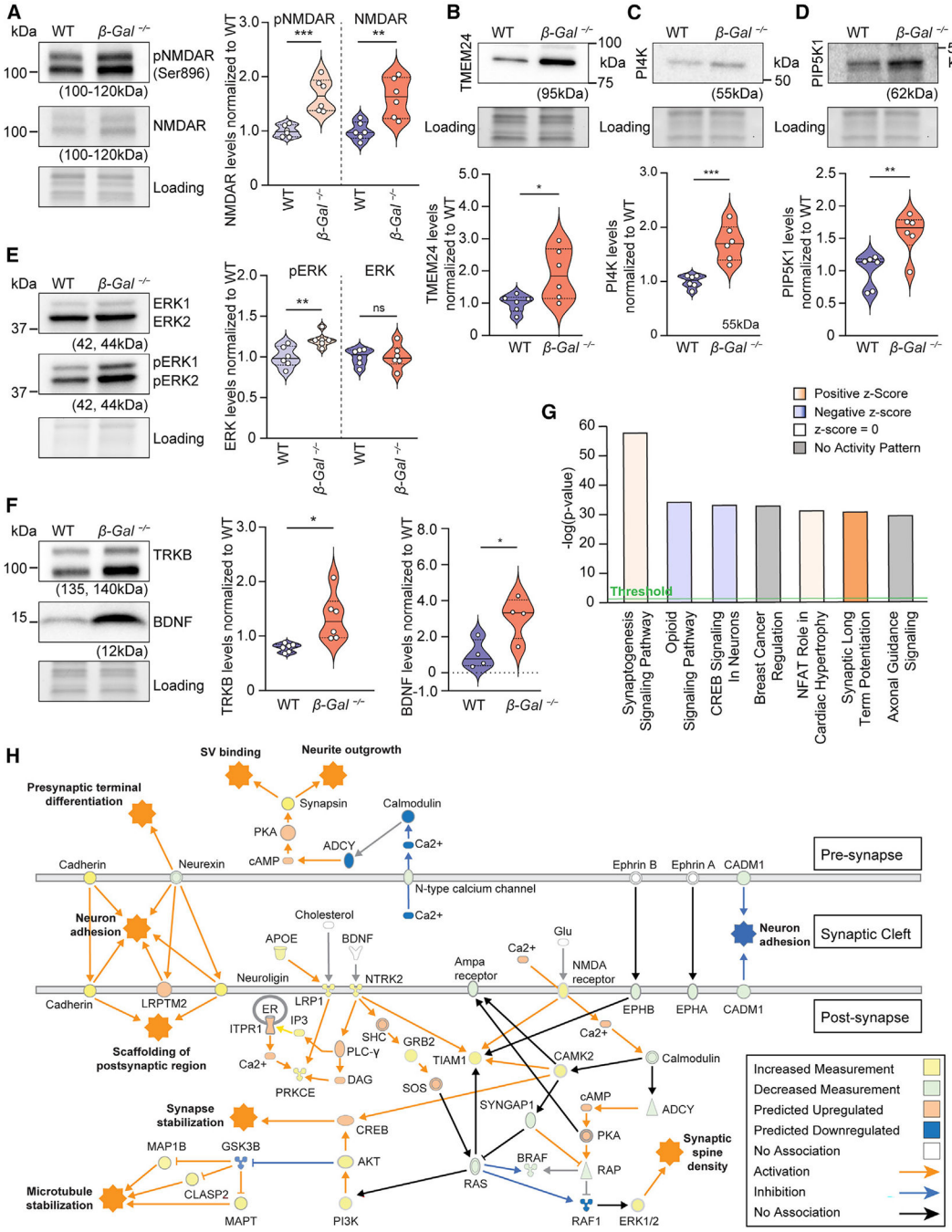

Figure 4. Increased levels of synaptic proteins in *β-Gal*$^{-/-}$ ER-PM junctions predict activation of the synaptogenesis-signaling pathway

(A–F) Representative immunoblots and quantification of (A) NMDAR type 1 subunit and pNMDAR ($n = 6$), (B) TMEM24 ($n = 6$), (C) PI4K ($n = 6$), (D) PIP5K1 ($n = 6$), (E) ERK1/2 and pERK1/2 ($n = 6$), and (F) TRKB ($n = 6$) and BDNF ($n = 4$) in WT and *β-Gal*$^{-/-}$ ER-PM junctions isolated from 6-month-old mice. Values are expressed as median ± quartiles. Statistical analysis was performed using the Student's t test; ns, not significant; *$p < 0.05$, **$p < 0.01$, ***$p < 0.001$.

(G) Graphical representation of pathways predicted to be upregulated (orange), downregulated (blue), or dysregulated with no predicted direction (gray), as determined by pathway analysis of proteomics data from ER-PM junctions isolated from 6-month-old WT and β-*Gal*$^{-/-}$ mice. Threshold = $-\log(p = 0.05)$.

(H) Network map showing proteins in the synaptogenesis-signaling pathway that were identified in the proteomic analysis of ER-PM junctions from WT and β-*Gal*$^{-/-}$ mice.

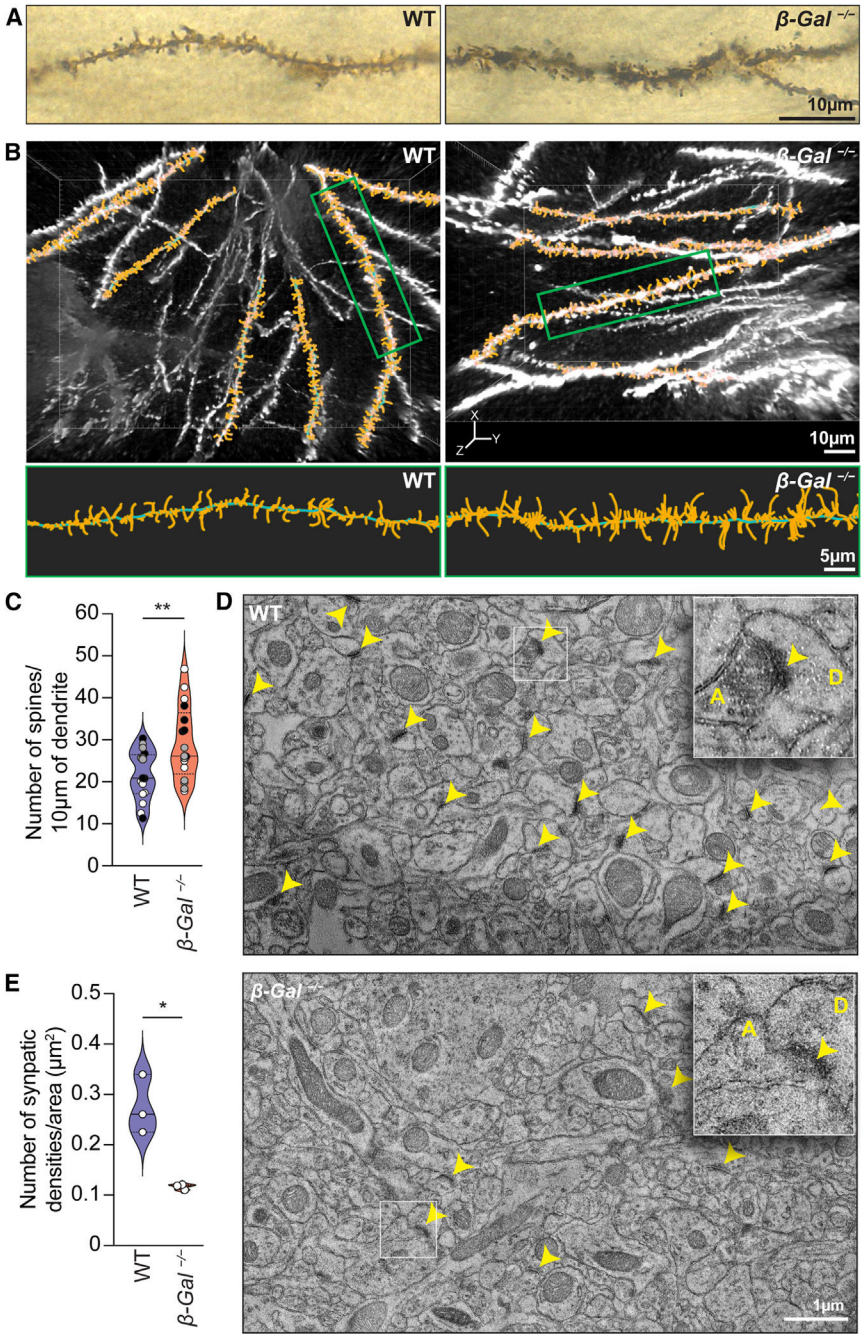

Figure 5. *β-Gal*$^{-/-}$ mice have an increased number of dendritic spines but decreased synaptic densities

(A) Golgi-Cox staining of dendritic branches and spines on hippocampal neurons from 6-month-old WT and *β-Gal*$^{-/-}$ mice. Scale bar: 10 μm.

(B) Three-dimensional (3D) reconstruction of optically sectioned Golgi-Cox-stained dendritic arbors of hippocampal pyramidal cells from 6-month-old WT and *β-Gal*$^{-/-}$ mice using Imaris Imaging software. Scale bar: 10 μm. Lower images show 2× zoom of highlighted regions (green boxes) in upper images. Reconstructed dendritic branches (green) and spines (orange) are shown. Scale bar: 5 μm.

(C) Quantification of the number of spines per length of dendrite from the 3D reconstruction in (B). WT $n = 16$ and $\beta\text{-}Gal^{-/-}$ $n = 17$ neurons; three mice, five or six images per mouse, each mouse is represented by a different colored filled datapoint (black, gray, white). Values are expressed as median ± quartiles. Statistical analysis was performed using the Student's t test; $^{**}p < 0.01$.

(D) TEM images of hippocampal pyramidal cell dendritic arbors from 6-month-old WT and $\beta\text{-}Gal^{-/-}$ mice. Synaptic densities are labeled by yellow arrows. Scale bar: 1 μm. Inset images show 3× zoom of white boxes. A, axon; D, dendrite.

(E) Quantification of the synaptic densities per field of view along the dendritic arbors of CA2 pyramidal cells shown in (D). $n = 3$; three mice, 12–15 fields of view along dendritic arbors of CA2 pyramidal cells per mouse. Values are expressed as median ± quartiles. Statistical analysis was performed using the Student's t test with Welch's correction; $^{*}p < 0.05$.

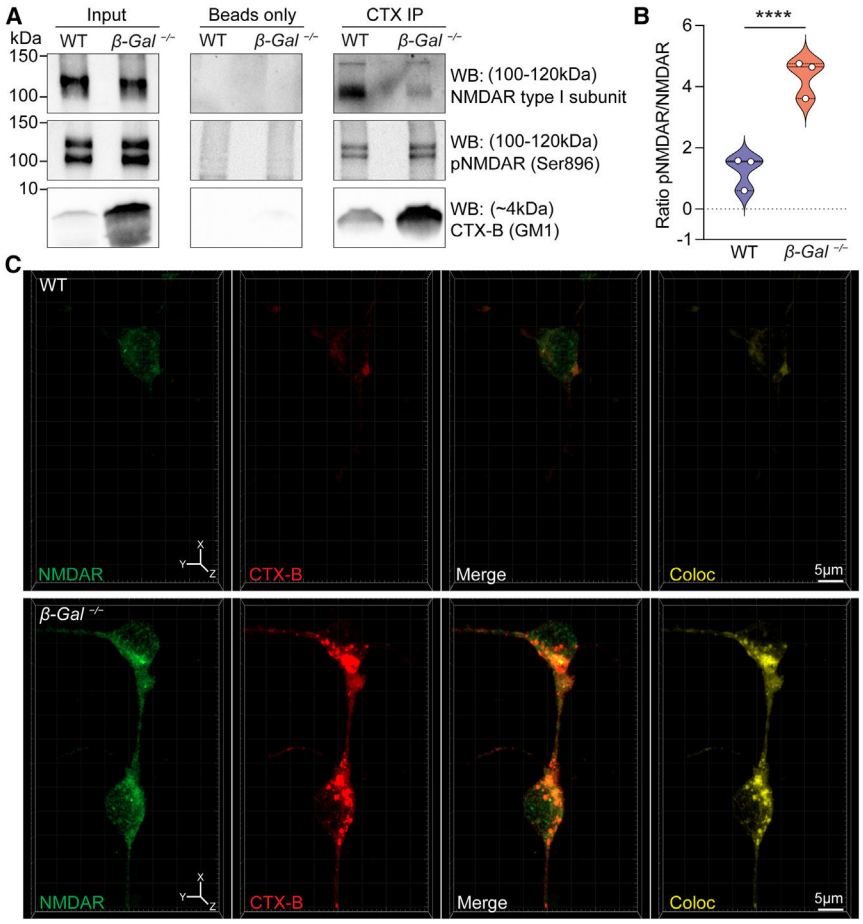

Figure 6. GM1 binds active pNMDAR within *β-Gal*$^{-/-}$ ER-PM junctions

(A) Immunoblots of coIP using cholera toxin B (CTX-B)-conjugated beads to pull down GM1 and bound proteins, NMDAR type 1 subunit and pNMDAR, in ER-PM junctions isolated from 6-month-old WT and *β-Gal*$^{-/-}$ mice.

(B) Quantification of the ratio of pNMDAR (Ser896) to NMDAR type 1 subunit measured in CTX-B coIP immunoblots; $n = 3$. Values are expressed as median ± quartiles. Statistical analysis was performed using the Student's t test with Welch's correction; ****$p < 0.0001$.

(C) z stacked immunofluorescence images of primary neurons isolated from P5 WT and *β-Gal*$^{-/-}$ brains, stained with CTX-B (GM1; red) and antiNMDAR type 1 subunit antibody (green). The co-localization (Coloc) channel shows the generated overlay of GM1 and NMDAR type 1 subunit staining using Imaris Imaging software. Scale bars: 5 μm.

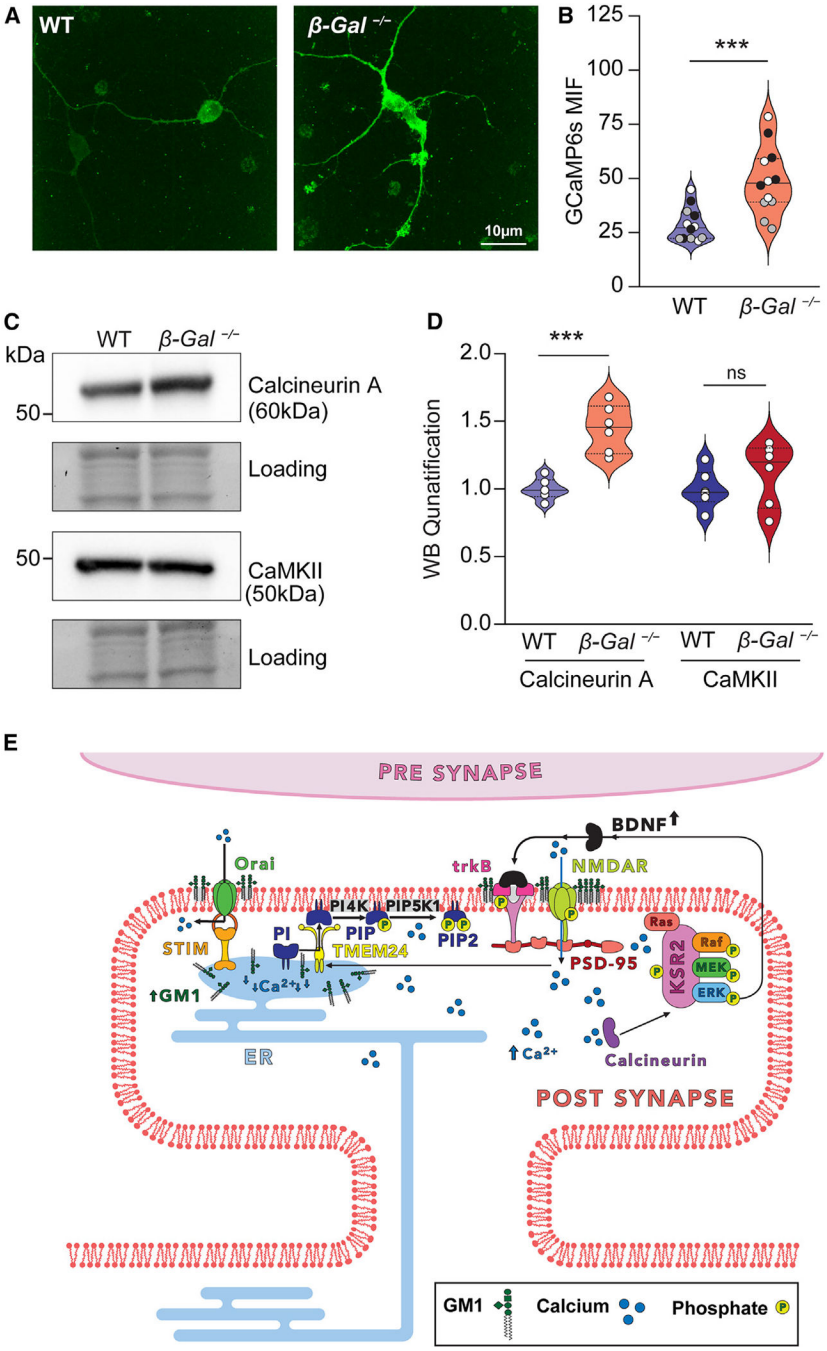

Figure 7. Primary *β-Gal*$^{-/-}$ neurons have increased intracellular Ca^{2+} concentration

(A) Fluorescence live-cell Ca^{2+} imaging using the genetically encoded Ca^{2+} sensor, GCamp6s, transduced in primary neurons isolated from the brains of P5 WT and *β-Gal*$^{-/-}$ mice. Scale bar: 10 μm.

(B) Quantification of the average fluorescence intensity of GCamp6s in primary neurons. $n = 12$, three mice with four wells per brain. Each mouse is represented by a different colored filled datapoint (black, gray, white). Values are expressed as median ± quartiles. Statistical analysis was performed using the Student's t test; ***$p < 0.001$.

(C) Representative immunoblots of calcineurin A and CaMKII in ER-PM junctions isolated from the brains of 6-month-old WT and β-*Gal*$^{-/-}$ mice.

(D) Quantification of immunoblots in (C). $n = 6$. Values are expressed as median ± quartiles. Statistical analysis was performed using the Student's t test; ns, not significant; ***$p < 0.001$.

(E) Model of the downstream effects of GM1 accumulation in β-*Gal*$^{-/-}$ ER-PM junctions: increased cytosolic Ca^{2+} levels through activation of pNMDARs influence the localization of TMEM24 to these MCSs, which mediates the transfer of phosphoinositides (PIs) to the PM. This pool of PIs can then be converted into the signaling molecules, phosphatidylinositol-4-phosphate (PIP) and phosphatidylinositol 4,5-bisphosphate (PIP2), which, in turn, change the synaptic architecture and increase NMDAR PM expression.[63,64] Concomitantly, increased concentration of cytosolic Ca^{2+} activates calcineurin-dependent ERK signaling, which is ‚necessary for BDNF production. Finally, BDNF activates TrkB, which, together with increased NMDARs, induces dendritic spine formation.

KEY RESOURCES TABLE

REAGENT or RESOURCE	SOURCE	IDENTIFIER
Antibodies		
Rabbit monoclonal anti-BDNF antibody	Abcam	Cat #: ab108319; RRID: AB_10862052
Rabbit anti-pan calcineurin A antibody	Cell Signaling	Cat #: 2614; RRID: AB_2168458
Rabbit polyclonal anti-calnexin antibody	Novus Biologicals	Cat #: NB100–1965; RRID: AB_10002123
Mouse monoclonal anti-CaMKII alpha (A-1) antibody	Santa Cruz	Cat #: Sc-13141; RRID: AB_626789
Rabbit monoclonal anti-p44/42 (ERK1/2) antibody	Cell Signaling	Cat #: 4695; RRID: AB_390779
Mouse monoclonal anti-flotillin-1 antibody	BD Biosciences	Cat #: 610820; RRID: AB_398139
Rabbit anti-Laminin A/C antibody	Cell Signaling	Cat #: 2032; RRID: AB_2136278
Goat anti-LDH antibody	Chemicon Intl.	Cat #: AB1222; RRID: AB_90491
Mouse anti–N-Cadherin antibody	BD Biosciences	Cat #: 610921; RRID: AB_398236
Rabbit monoclonal anti-NMDA Receptor 1 antibody	Cell Signaling	Cat #: 5704; RRID: AB_1904067
Rabbit polyclonal anti-ORAI1 antibody	Abcam	Cat #: ab86748; RRID: AB_10672921
Mouse monoclonal anti-phospho-p44/42 (ERK1/2) (thr202/Tyr204) antibody	Cell Signaling	Cat #: 9106; RRID: AB_331768
Rabbit anti-PI4 Kinase antibody	Cell Signaling	Cat #: 4902; RRID: AB_2164029
Rabbit anti-PIP5K1A antibody	Cell Signaling	Cat #: 9693; RRID: AB_2164698
Rabbit polyclonal anti-phospho-NMDAR (Ser896) antibody	Invitrogen	Cat #: PA5–37589; RRID: AB_2554197
Rabbit anti-PSD-95	Cell Signaling	Cat #: 3450; RRID: AB_2292883
Rabbit anti-STIM1 antibody	Cell Signaling	Cat #: 4916; RRID: AB_2271287
Rabbit anti-STIM2 antibody	Cell Signaling	Cat #: 4917; RRID: AB_2198021
Guinea pig anti-Synaptophysin 1 antibody	Synaptic Systems	Cat #: 101 004; RRID: AB_1210382
Rabbit polyclonal anti-TMEM24 antibody	Fitzgerald	Cat #: 70R-7325; RRID:AB_10814391
Mouse monoclonal anti-TOMM20 antibody	Santa Cruz	Cat #: sc-11415; RRID: AB_2207533
Rabbit monoclonal anti-TRKB antibody	Cell Signaling	Cat #: 4603; RRID: AB_2155125
Rabbit polyclonal anti-VAP-33 (VAPA) antibody	Bethyl	Cat #: A304–366A; RRID: AB_2620561
Rabbit polyclonal anti VAPB antibody	Bethyl	Cat #: A302–894A; RRID: AB_10663774
Cholera toxin subunit B Biotin-conjugated	Invitrogen	Cat #: C34779
Cholera toxin subunit B Alexa Fluor™ 555-conjugated	Invitrogen	Cat #: C34776
Cholera toxin subunit B HRP-conjugated	Invitrogen	Cat #: C34780

REAGENT or RESOURCE	SOURCE	IDENTIFIER
Donkey anti-Rabbit Alexa Fluor™ 488-conjugated IgG	Invitrogen	Cat #: A21206; RRID: AB_2535792
Goat anti-Rabbit Alexa Fluor™ 568-conjugated IgG	Invitrogen	Cat #: A11036; RRID: AB_10563566
Goat anti-Gunea Pig Alexa Fluor™ 488-conjugated IgG	Invitrogen	Cat #: A11073; RRID: AB_2534117
Bacterial and virus strains		
GFP-MAPPER	Gift from Jen Liou's lab (Chang et al.)[49]	Addgene #117721
pGP-CMV-GCAMP6s	Gift from Douglas Kim's lab (Chen et al.)[73]	Addgene #40753
tdTomato-Calreticulin-N-16	Gift from Michael Davidson's lab	Addgene #58074
Chemicals, peptides, and recombinant proteins		
GM1 isolated from bovine brain	Millipore Sigma	G7641
Protein A Magnetic Beads	Cell Signaling	73778S
NanoLINK Strepdaviden Magnetic Beads	Vector Labs	M-1002–010
Critical commercial assays		
FD Rapid GolgiStain™ Kit	FD NeuroTechnologies	PK401
Deposited data		
ER-PM junction proteomics data	This study	PXD042994
Experimental models: Cell lines		
HeLa	ATCC	CRM-CCL-2
HEK293T	ATCC	CRL-3216
Experimental models: Organisms/strains		
B6.129P2(FVB)-*Glb1*^{tm1Adz}/J (*β-Gal*$^{-/-}$)	Jackson Labs	Strain #:037063
Software and algorithms		
ImageJ	Schneider et al.[74]	https://imagej.net/ij/download.html
Imaris Analysis Software	Oxford Instruments	https://imaris.oxinst.com/products/imaris-for-neuroscientists

Cell Rep. Author manuscript; available in PMC 2024 July 12.

REAGENT or RESOURCE	SOURCE	IDENTIFIER
IMOD software	Kremer et al.[75]	https://bio3d.colorado.edu/imod/download.html
SerialEM Software	David Mastronarde[76]	https://bio3d.colorado.edu/SerialEM/
Other		
Pansorbin Cells	Millipore Sigma	507858–1GM